Faculty of Sciences
Department of Physics

Structural Mechanisms of Ferroelectricity and Ferroelasticity in Compounds with the Formula: β'-$RE_2(MoO_4)_3$

FINAL DEGREE PROJECT (2024-2025)

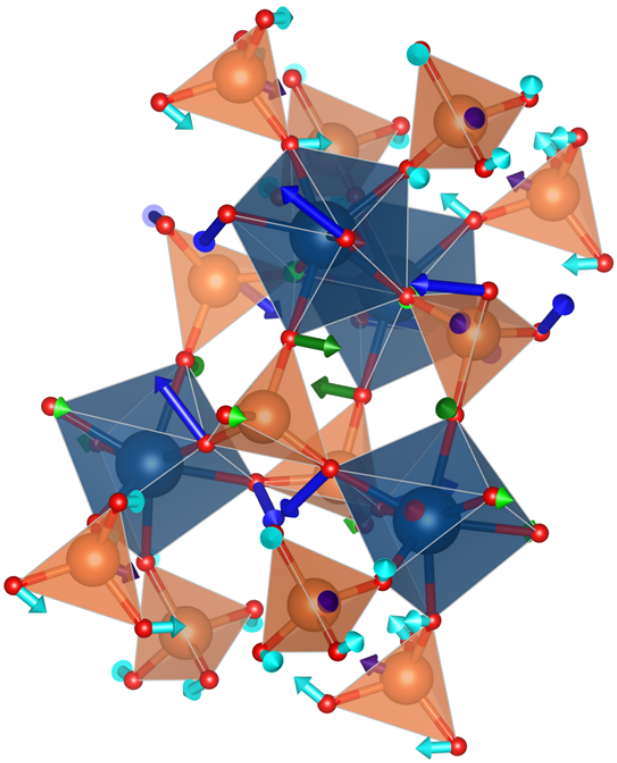

Author: Alberto Reyes Castro

Supervised by: María Cristina González Silgo, Gerardo Gil de Cos.

Abstract

Rare-earth trimolybdates $RE_2(MoO_4)_3$ (RE = Tb, Dy, Ho) constitute a model system for the study of improper ferroelectricity associated with low-symmetry structural transitions. This work analyzes the temperature evolution of the β (paraelectric–paraelastic) and β' (ferroelectric–ferroelastic) phases, evaluating the effect of ionic radius on crystal distortion throughout this transition. High-resolution X-ray and neutron diffraction data were collected in the 225–475 K range and refined using the Rietveld and Le Bail methods, complemented by a detailed distortion-mode analysis to quantify the amplitudes of primary nonpolar and secondary polar modes (amplimodes). The combination of both diffraction techniques enabled a more complete structural characterization, taking advantage of the differential sensitivity of X-rays to heavy elements and neutrons to oxygen. Additionally, atomic displacements associated with these modes were compared with theoretical calculations, exploring the relative influence of chemical pressure induced by ionic substitution versus hydrostatic pressure and thermal evolution. The results provide a detailed view of the possible structural mechanisms involved in these improper ferroelectric and ferroelastic transitions, particularly those dominated by the primary mode. The reliability of the conclusions regarding the structural behavior of the three compounds is supported by the quality of the refinements, although secondary modes proved more difficult to interpret. This work provides a framework for future studies aimed at optimizing and designing ferroic materials, as well as coupling and controlling their properties.

Acknowledgements

I would like to express my sincere gratitude to my Final Degree Project supervisors, Dr. María Cristina González Silgo and Dr. Gerardo Gil de Cos, for their expert guidance, valuable suggestions and constant support throughout this project.

I am also grateful to the CCDD research group (Crecimiento, Caracterización y Difracción de Materiales Dieléctricos) at the University of La Laguna, which provided access to its facilities, shared its expertise and fostered a genuinely collaborative research environment.

I would like to acknowledge the Institut Laue–Langevin (ILL) for providing the neutron diffraction data and technical support during the D2B experimental campaign. I also acknowledge the support of the X-ray Diffraction Service of the CAI at the Complutense University of Madrid.

Finally, I would like to thank my classmates, friends and family for their support and encouragement throughout this work.

Contents

1 Introduction

Chapter 1 Summary

This work, framed within the research line of the CCDD group, focuses on the detailed analysis of the structural transition $\beta \rightarrow \beta'$ in compounds with $RE = Tb$, Dy and Ho, with the aim of evaluating how the ionic radius affects structural stability and the emergence of polarization. In this type of ferroic transition, ferroelectricity is improper: it does not arise directly from a dominant polar mode, but is induced through coupling with nonpolar structural modes that act as primary order parameters. To describe this phenomenon accurately, the theoretical framework of group–subgroup relations is used, introducing amplimode analysis as a way to decompose the total crystal distortion into static normal modes associated with irreducible representations of the high-symmetry phase. This approach makes it possible not only to identify and quantify the primary modes responsible for symmetry breaking, but also the secondary modes responsible for polarization. In this way, a structurally grounded strategy is proposed to understand the origin of improper ferroelectricity and guide the rational design of new multifunctional materials, integrating concepts from crystallography, solid-state physics and symmetry theory.

1.1 Introduction to Ferroic Materials: Ferroelectricity and Ferroelasticity

The development of materials with advanced functional properties is a cornerstone of modern materials science. Such materials play a critical role in areas including energy storage[1], energy harvesting and conversion[2], efficient sensing[3], advanced lighting[4], and information processing[5]. Among these, ferroic materials are of particular interest due to their ability to exhibit spontaneous orderings in response to external stimuli[6].

Ferroic materials are primarily classified as ferromagnetic, ferroelectric, or ferroelastic, depending on the type of spontaneous ordering they exhibit: magnetization, electric polarization, or mechanical strain, respectively. In many cases, these orderings are coupled, giving rise to multiferroic compounds that combine multiple ferroic properties and open new avenues for multifunctional devices.

The hallmark of ferroic behavior lies in a material's crystal structure. A change in structural symmetry can trigger a ferroic phase transition, typically driven by an external parameter such as temperature, pressure, or electric field. These transitions involve a transformation from a high-symmetry (para-phase) to a lower-symmetry (ferro-phase), accompanied by the emergence of a spontaneous order parameter. For instance, in ferroelectric materials, this parameter is the spontaneous polarization; in ferroelastic materials, it is the spontaneous strain[7].

1.1.1 Ferroelectric Materials

Ferroelectric materials are those that exhibit a spontaneous electric polarization, which can be reversed by applying an external electric field. This property arises in non-centrosymmetric structures, where the centers of positive and negative charge do not coincide, creating permanent electric dipoles. For such polarization to occur, the crystal structure must possess a polar axis. During a ferroelectric phase transition, the material changes from a paraelectric phase (high symmetry, no spontaneous polarization) to a ferroelectric phase (low symmetry, with spontaneous polarization). This polarization can align along multiple equivalent directions, giving rise to ferroelectric domains and hysteresis phenomena when cyclic electric fields are applied.

This switching capability underpins applications such as memory devices and piezoelectric and pyroelectric actuators. A prominent feature of ferroelectrics is their high dielectric permittivity, particularly near the transition point, which makes them excellent materials for capacitors. Moreover, their coupling with other physical properties enables integration into multifunctional devices combining sensing, energy storage, and actuation[8].

1.1.2 Ferroelastic Materials

Ferroelastic materials exhibit spontaneous strain under certain conditions, and their shape can be reoriented by applying mechanical stress. This strain is associated with a reversible structural transition that involves a change in the crystal's directional symmetry; as in ferroelectrics, this transition generates domains—in this case, ferroelastic domains—and displays hysteresis when plotting strain versus applied stress. This property has been extensively explored for applications such as shape-memory materials, stress sensors, and smart actuators, particularly in the fields of soft robotics and bioinspired systems. It is important to emphasize that ferroelasticity can exist independently, without coexisting with other ferroic properties; however, its coupling with ferroelectricity is common, especially in perovskite compounds where strain and polarization are activated simultaneously[9].

1.1.3 Structure–Property Relationship: A Crystallographic Approach

Understanding the relationship between atomic structure and the physical properties of ferroic materials has been a fundamental research focus; the pioneering work of Professor S. C. Abrahams in X-ray and neutron diffraction enabled highly precise quantification of atomic positions, contributing to the understanding of how subtle structural distortions give rise to phenomena such as piezoelectricity, pyroelectricity, ferroelectricity, and ferroelasticity. Thanks to these studies[10], we now know that the nature and orientation of the order parameter, as well as the transition pathways between different structural phases, directly determine the macroscopic properties of materials; for example, the symmetry of the space group dictates the possibility of having a polar axis, and the presence of certain vibrational modes can spontaneously induce a structural rearrangement that triggers the ferroic property.

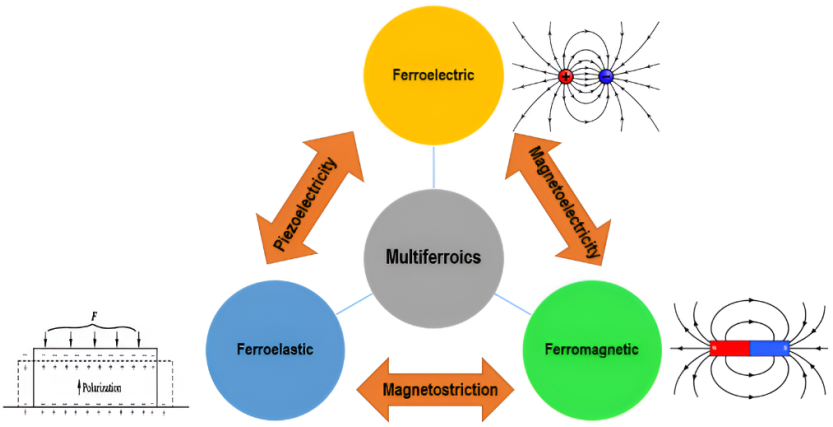

Figure 1: Schematic representation of the relationships between ferroic properties in multiferroic materials[7]. The interplay between ferroelectric, ferromagnetic and ferroelastic orders gives rise to functional couplings such as piezoelectricity, magnetoelectricity and magnetostriction, reflecting how subtle structural distortions can induce emergent macroscopic properties.

1.2 Rare-Earth Molybdates, Specifically of the β'-$RE_2(MoO_4)_3$ Type (RE = Rare Earth Elements)

The present research focuses on the family of compounds with general formula $RE_2(MoO_4)_3$, where RE denotes a rare-earth element. These trimolybdates constitute a class of materials of notable interest due to their structural diversity, complexity of phase transitions, and functional potential in optoelectronics and ferroic materials science. Members of this series crystallize into different polymorphic phases—α, β, β' and γ—depending on factors such as the lanthanide ionic radius, temperature, pressure, and synthesis conditions (e.g., reaction time and calcination temperature). This crystallographic versatility endows these materials with rich structural and functional properties. The first $RE_2(MoO_4)_3$ compounds were synthesized by Hitchcock in 1895, specifically the molybdates of lanthanum, praseodymium, and neodymium[11]. However, the key discovery in this series occurred in 1966, when Borchardt and Bierstedt synthesized $Gd_2(MoO_4)_3$ and observed its ferroelectric behavior for the first time, marking the beginning of growing interest in ferroic trimolybdates[12].

1.2.1 Structural Diversity and Phase Transitions

Rare-earth molybdates exhibit significant structural flexibility, enabling them to undergo phase transitions induced by external stimuli. The main phases are:

- **Phase α (RE = La–Dy)**: stable at room temperature in compounds with intermediate-radius lanthanides. It exhibits complex modulated structures related to chelites, which significantly influence its physical properties. These structures can transform under pressure or temperature into the β or γ phases, with applications in lasers, LEDs, sensors, detectors, photocatalysts, etc.[13]
- **Phases β and β' (RE = Pr–Ho and Y)**: both are non-centrosymmetric and of special interest for nonlinear optics. Phase β can transform into phase β' (ferroelectric and ferroelastic, of lower symmetry and polar) upon cooling, which involves a structural distortion that breaks symmetry and generates spontaneous polarization and strain. These phases have potential applications in nonlinear optics (e.g., second-harmonic generation)[12;14].
- **Phase γ (RE = Ho–Lu and Y)**: appears in molybdates with lighter rare-earth ions (smaller ionic radius). Its structure differs from the previous ones and is characterized by phenomena such as negative thermal expansion, with applications in thermal management materials[15;16].

1.2.2 Research Context

The CCDD research group (Crecimiento, Caracterización y Difracción de Materiales Dieléctricos) at the University of La Laguna has developed an extensive program focused on $RE_2(MO_4)_3$ compounds (RE = lanthanides and yttrium; M = Mo, W). Their studies have covered key aspects such as mechanisms of negative thermal expansion[17], correlations between temperature-dependent crystal structure and various electrical transport mechanisms—electronic, ionic, and polaronic—[18], comparisons between the effects of chemical substitution and high physical pressure[19], and the optimization of luminescent properties[20].

This research is situated within that framework and focuses on analyzing the β and β' phases, their structural stability, temperature evolution, and the $\beta \rightarrow \beta'$ structural transition. Understanding the relationships between structure, symmetry, and physical properties is essential for advancing synthesis optimization and the rational design of these functional materials.

1.3 Motivations and Objectives of the Work and Structure

1.3.1 Motivations and Objectives

This work is framed within the research program of the CCDD group, with the general objective of deepening our understanding of the structural mechanisms governing the phase transitions in these compounds and their relationship with the emergence of spontaneous polarization and ferroelastic strain.

A distinctive feature of the β' phases is their improper ferroelectric character, where the polarization does not arise as a primary order parameter, but as a consequence of coupling with another dominant structural parameter, such as a nonpolar lattice distortion, charge ordering, or spin ordering. This type of coupling enables the emergence of unconventional functional properties, broadening the range of response to external stimuli and opening new possibilities for the design of functional materials for future electronics[21;22].

Since the first studies on $Gd_2(MoO_4)_3$, where the ferroelastic–ferroelectric transition was attributed to an order–disorder mechanism accompanied by a "soft mode"[23], significant progress has been made in understanding these systems.

In this pioneering study a maximum oxygen-atom displacement of only 0.7 Å was identified and a spontaneous polarization consistent with experimental data ($P_s \approx 0.175\ \mu C\,cm^{-2}$) was estimated, particularly associated with the oxygen displacements determined by single-crystal X-ray diffraction.

However, more recent work, such as that of Nylund *et al.*[24], has revealed greater complexity in the transition mechanisms: using Rietveld refinements of X-ray thermodiffraction data on powder samples, it was shown that the different cations in $Gd_2(MoO_4)_3$ follow qualitatively distinct behaviors in each crystallographic layer, with atomic displacements that not only correlate with the macroscopic strain but also introduce hidden degrees of freedom that shed new light on the microscopic origin of spontaneous polarization in these improper ferroelectrics.

In this context, the CCDD group has made significant contributions to the study of the $RE_2(MoO_4)_3$ family through a detailed structural approach. For example, Guzmán-Afonso analyzed the relationship between structural distortions and ionic radii in various molybdates, demonstrating how the ferroelastic –ferroelectric order parameter varies with the nature of the rare earth[25].

Subsequently, in the study of $Ho_2(MoO_4)_3$[26], thermal transitions among three phases ($\beta' \rightarrow \beta \rightarrow \gamma$) were identified, including both reversible and irreversible transformations.

More recently, Gil-de-Cos *et al.*[27] characterized $Y_2(MoO_4)_3$ from a comprehensive structural and ferroelectric perspective, including the experimental observation of hysteresis loops and the correlation between the symmetry modes involved in the transition and the macroscopic electrical parameters.

The study that most directly inspires this work is the one carried out by the CCDD group on the $La_xEr_{2-x}(MoO_4)_3$ solid solution, in which the correlation between crystal structure and ferroelectric properties was analyzed via X-ray diffraction and Rietveld refinements with symmetry-mode analysis[28].

One of the main methodological contributions was the use of the `AMPLIMODES` software[29] to decompose the structural distortion into symmetry modes, quantitatively identifying the order parameters involved in the transition. Unexpectedly, an increase in spontaneous polarization and Curie temperature was observed with increasing Er^{3+} concentration (i.e., decreasing average ionic radius), in contrast with the usual trend in $RE_2(MoO_4)_3$ molybdates.

This result suggests a more complex structural and ferroelectric behaviour, and a greater tunability of properties in these materials, motivating the comparative study of systems with consecutive rare-earth ionic radii.

In this context, the main objective of this thesis is to study the structural stability and phase transitions in β'-$RE_2(MoO_4)_3$ molybdates with RE = Tb, Dy and Ho, taking advantage of the proximity and consecutiveness of their ionic radii to explore the influence of cation size on improper ferroelectricity.

To this end, experimental X-ray and neutron diffraction data will be analysed by Rietveld refinements using the `AMPLIMODES` software, in order to differentiate between the primary and secondary order parameters governing the transition.

A key aspect will be comparing RE and Mo cation displacements with those of oxygen anions, to identify the main structural actors in the development of spontaneous polarization and strain.

Moreover, with available *ab initio* calculations for $Tb_2(MoO_4)_3$[30], the influence of chemical pressure induced by cation substitution can be contrasted with hydrostatic pressure, thus providing a more complete view of the factors modulating the transition.

Finally, this work also has an academic and formative objective, framed within the BSc in Physics: to deepen expertise in key areas such as crystallography, solid-state physics, X-ray and neutron diffraction techniques, and structural phase transitions, integrating foundational knowledge from various BSc courses, including among many others: **Electromagnetism**, **Solid State Physics**, **Materials Characterization**, **Statistical Physics**, and **Physical Optics**.

1.3.2 Structure of the Work

This work is structured in five main chapters—Introduction, Methodology I, Methodology II, Results Analysis and Discussion, and Conclusions and Future Work—following the typical research format. However, it adopts a progressive approach that starts with fundamental concepts and advances towards more specific topics, less covered in the BSc in Physics. The study culminates with the analysis and interpretation of real diffraction data.

This sequence not only aims to facilitate understanding of the investigated physical and structural phenomenon, but also to reflect the learning and development process undertaken throughout the completion of the Final Degree Project.

Within this structure, the Methodology II chapter, dedicated to Rietveld refinement, stands out as the core of the work, which received the majority of time and effort. Although the experimental data acquisition (described in Methodology I) was not directly conducted by the author, a detailed explanation of the procedure is included for its educational value. Finally, the most relevant results are presented and analysed, leaving possible future research lines outlined.

1.4 Fundamentals of Symmetry and Crystallography for Structural Analysis

1.4.1 Direct Lattice and Symmetry Elements

Crystalline materials exhibit a three-dimensional periodic arrangement of atoms, described by a crystal lattice: an infinite array of points in space generated by integer translations of a set of basis vectors $\vec{a}, \vec{b}, \vec{c}$. These vectors define the unit cell, which, when repeated, generates the entire crystal structure.

If the cell contains a single lattice point, it is called *primitive*; if it contains additional lattice points (at the body center or faces), it is called *centered*. In addition to translations, crystals can exhibit symmetry operations that relate equivalent positions: rotations, reflections, inversions, rotoinversions, screw axes, and glide planes.

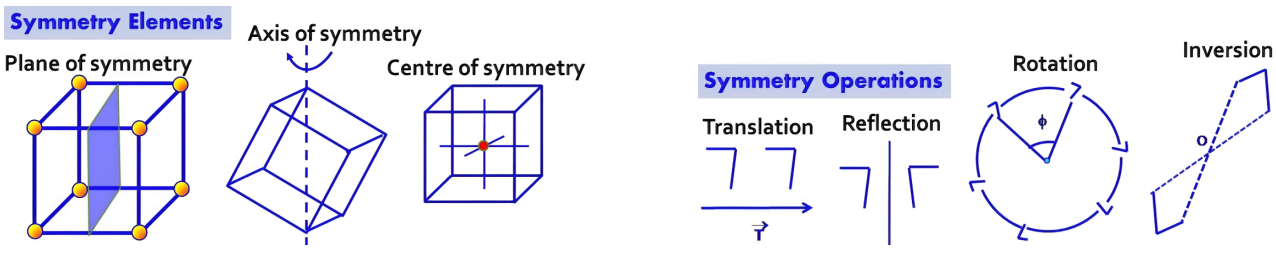

Figure 2: Schematic of symmetry in a crystal lattice: (Left) symmetry elements—rotation axes, reflection planes, and inversion centers—are shown. (Right) symmetry operations together with the translations defined by the basis vectors $\vec{a}$, $\vec{b}$, and $\vec{c}$, which generate the three-dimensional periodic structure of the crystal[31].

These transformations are expressed by matrices R acting on the position vectors, $\vec{r}\,' = R \cdot \vec{r}$, distinguishing operations that preserve chirality (such as rotations and translations) from those that invert it (such as reflections or inversions).

1.4.2 Point Groups, Space Groups, and Structural Elements

Crystal classes, or point groups, are combinations of symmetry operations that leave at least one point fixed and are compatible with the crystal's periodicity. There are 32 point groups, organized into seven crystal systems (cubic, tetragonal, hexagonal, trigonal, orthorhombic, monoclinic, and triclinic). When these systems are combined with the possible centering types, they yield the 14 Bravais lattices[32].

To fully describe a crystal's symmetry, one uses the space group, which incorporates both point symmetries and translational symmetries (pure translations, screw axes, and glide planes). There are 230 unique space groups in 3D, each of which unambiguously defines the crystal's internal organization.

A crystal structure is completely specified by its space group and its asymmetric unit, i.e., the minimal set of independent atomic positions from which all unit-cell positions are generated by applying the space-group operations.

These positions are grouped into sets called Wyckoff positions, characterized by their multiplicity (the number of positions generated from a single one) and their local site symmetry. The number Z indicates how many formula units the full unit cell contains and is related to the multiplicities of the occupied Wyckoff sites and the lattice type. Positions may be general (no local symmetry) or special (lying on symmetry elements and having fixed coordinate constraints).

1.4.3 Reciprocal Lattice, Miller Indices, and Brillouin Zones

Miller indices (hkl) are used in crystallography to identify sets of equivalent crystal planes, i.e., families of regularly spaced parallel planes that can be described in any direct lattice. These integer indices are obtained from the intercepts of each plane with the crystal axes. Different notations are used depending on context: (hkl) denotes a specific plane, $\{hkl\}$ a family of symmetry-equivalent planes, and $[hkl]$ a crystallographic direction (perpendicular to the plane).

To study wave propagation in crystals—whether electronic, vibrational, or electromagnetic—the *reciprocal lattice* is used, a geometric construction that translates the crystal's periodicity into momentum space. Each set of Miller indices (hkl) defines a family of real-space planes and is associated with a reciprocal-lattice vector:

$$\vec{G}_{hkl} \;=\; h\,\vec{a}^{*} \;+\; k\,\vec{b}^{*} \;+\; l\,\vec{c}^{*} \tag{1.1}$$

Thus, each point in the reciprocal lattice represents a family of crystal planes, and the vectors connecting these points are directly related to diffraction processes and the conservation of crystal momentum in solid-state interactions[32]. The reciprocal-lattice basis vectors $\vec{a}^{*}$, $\vec{b}^{*}$, $\vec{c}^{*}$ are related to the direct-lattice vectors by:

$$\vec{a}^{*} = \frac{\vec{b}\times\vec{c}}{V}, \quad \vec{b}^{*} = \frac{\vec{c}\times\vec{a}}{V}, \quad \vec{c}^{*} = \frac{\vec{a}\times\vec{b}}{V} \tag{1.2}$$

where V is the volume of the real-space unit cell.

The diffraction condition we will use in this work is **Bragg's law**, which gives the criterion for constructive interference of waves reflected (diffracted) by the crystal planes:

$$n\lambda = 2\,d_{hkl}\,\sin\theta \tag{1.3}$$

where λ is the wavelength of the incident radiation, n the diffraction order, d_{hkl} the interplanar spacing, and θ the incidence angle (see Fig. 3).

This condition can be reinterpreted in reciprocal-space via the **Laue condition**, which states that diffraction occurs when the change in wavevector equals a reciprocal-lattice vector:

$$\vec{k} - \vec{k}_0 = \vec{G}_{hkl} \tag{1.4}$$

Here, $\vec{k}_0$ (incident) and $\vec{k}$ (diffracted) are the wavevectors of the incoming and outgoing radiation, respectively. In this framework, **Bragg planes** are the planes perpendicular to $\vec{G}_{hkl}$ vectors, whose magnitude relates to the interplanar spacing by:

$$|\vec{G}_{hkl}| = \frac{2\pi}{d_{hkl}} \tag{1.5}$$

This illustrates how reciprocal-lattice geometry provides a precise and general criterion for predicting diffraction conditions, beyond the original Bragg formulation.

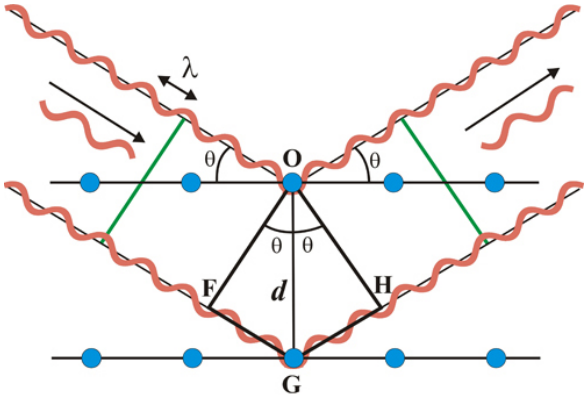

Figure 3: Visual representation of Bragg's law[33].

The *Wigner–Seitz cell* is the region of space closer to a given lattice point (e.g., the origin) than to any other lattice point. Its reciprocal-space analogue is the *first Brillouin zone*, defined as the set of points nearer the reciprocal-lattice origin than to any other reciprocal-lattice node. Higher-order zones (second, third, etc.) also play a central role in solid-state physics.

Wavevectors $\vec{k}$ lying inside or on the boundary of the first Brillouin zone correspond to allowed states in a periodic system, characterizing quantum states such as electronic bands or vibrational modes (phonons). For example, wavevectors at the zone center (the Γ point, with $\vec{k} = 0$) describe excitations with no phase variation between adjacent cells, whereas vectors at zone edges or corners represent states with more complex periodicities, often dictated by lattice symmetry. Thus, the Brillouin zone provides a natural framework for describing the physics of periodic systems and understanding how reciprocal-space structure influences their electronic and dynamical properties[32].

1.4.4 Group–Subgroup Relations and *Amplimodes*

The theory of group–subgroup relations allows one to understand how an ideal high-symmetry crystal structure, characterized by a space group G (parent phase), can transform into a lower-symmetry structure (child phase) associated with a subgroup $S < G$.

This symmetry reduction—typically subtle—is common in many structural phase transitions in real materials. Such transitions can be described as a sequence of symmetry-lowering steps, in which the symmetry is gradually reduced through maximal subgroups. These relationships are represented by hierarchical subgroup diagrams.

We distinguish two types of subgroups:

- **Translationengleich subgroups**: the daughter phase preserves the same translation lattice (the unit cell does not change) but loses part of its point symmetry.
- **Klassengleich subgroups**: some point symmetry is preserved, but the translation lattice changes—the unit cell expands and the number of independent atomic positions may increase.

In this context, *amplimodes* emerge as a fundamental tool to characterize the static structural distortions responsible for that symmetry reduction. Each *amplimode* represents a normal mode of collective atomic displacement within the unit cell, and can be directly associated with an irreducible representation of the high-symmetry point group[29].

Although *amplimodes* share a mathematical description similar to dynamic vibrational modes (phonons), their physical interpretation is different:

- **Phonons**: correspond to harmonic temporal oscillations of the crystal lattice, responsible for thermal transport and the dynamic properties of the solid.
- ***Amplimodes***: represent time-frozen displacements that describe the new structural configuration after a phase transition.

The identification of an *amplimode* begins with the symmetry analysis of the parent space group G, and is strongly conditioned by the Brillouin zone structure, especially at high-symmetry points such as Γ. In many cases, the relevant *amplimodes* are located at Γ, but they can also involve other reciprocal-space points if the distortion involves a nonzero wavevector, leading to a doubling or modulation of the unit cell.

The key idea is that each group–subgroup transition can be described as the activation of one or more *amplimodes*, whose superposition generates the lower-symmetry structure. In other words, the resulting structure is a systematic deformation of the high-symmetry state, in which atoms reorganize coherently according to patterns dictated by the symmetry of group G.

Each *amplimode* has a direction (polarization vector) and a magnitude (amplitude), which quantifies the degree of distortion. Mathematically, for a crystal with N atoms per unit cell, there are $3N$ degrees of freedom, and *amplimodes* allow any distortion to be decomposed into a basis of normal modes compatible with the symmetry. Thus, the transition from G to S is described not only abstractly in terms of subgroup relations, but also physically and quantitatively through the excitation of specific key *amplimodes*.

Hence, *amplimodes* serve as a bridge between space-group theory and the structural description of crystal phases, providing a robust foundation for understanding how new structures emerge from a high-symmetry phase, as well as their functional implications.

1.5 Description of the β and β' Phases of $RE_2(MoO_4)_3$

The crystalline β and β' phases of the rare-earth trimolybdates $RE_2(MoO_4)_3$ (RE = Sm–Ho) exhibit a clear structural and symmetry relationship that illustrates how ferroic phase transitions can be described via group–subgroup relations and distortion-mode (*amplimode*) analysis.

In both cases, the three-dimensional network is built from MoO_4 tetrahedra sharing vertices with REO_7 polyhedra, preserving the same atomic connectivity but with different degrees of symmetry and distortion (see Figs. 4 and 5).

1.5.1 Structure of the β Phase: High Symmetry and Paraelectric Configuration

The β phase crystallizes in the tetragonal system, with space group $P\bar{4}\,2_1\,m$ (No. 113), and contains $Z = 2$ formula units per cell. Its asymmetric unit includes two molybdenum atoms, one rare-earth atom, and four oxygen atoms.

One of the molybdenum atoms (Mo1) occupies the Wyckoff position $2a$, with elevated symmetry, located on a fourfold inversion axis. It is coordinated by four equivalent oxygens generated from O4, which lies on a general position, forming a regular tetrahedron.

The second molybdenum atom (Mo2), at position $4e$, lies on a mirror plane containing the c axis. It forms a slightly distorted tetrahedron with oxygens O1 and O2, also on the mirror plane, plus oxygen O3 in a general position, which generates the fourth vertex.

The rare-earth atom (RE), also in a $4e$ site, is coordinated by seven oxygens from seven distinct tetrahedra: one O1 on the mirror plane, two O2, two O3, and two O4—each pair generated by the mirror-plane symmetry. Two of these coordination polyhedra share an edge in a plane perpendicular to the c axis.
RE–O–Mo and RE–O–RE bridges complete a dense, robust three-dimensional network. This network can be viewed as layers stacked perpendicular to c, with Mo-dominated planes at $z = 0$ and $z = 1$, and the less symmetric Mo and RE at $z \approx \frac{1}{3}$ and $z \approx \frac{2}{3}$.

Despite being non-centrosymmetric, this phase is paraelectric and paraelastic, exhibiting nonlinear optical effects.

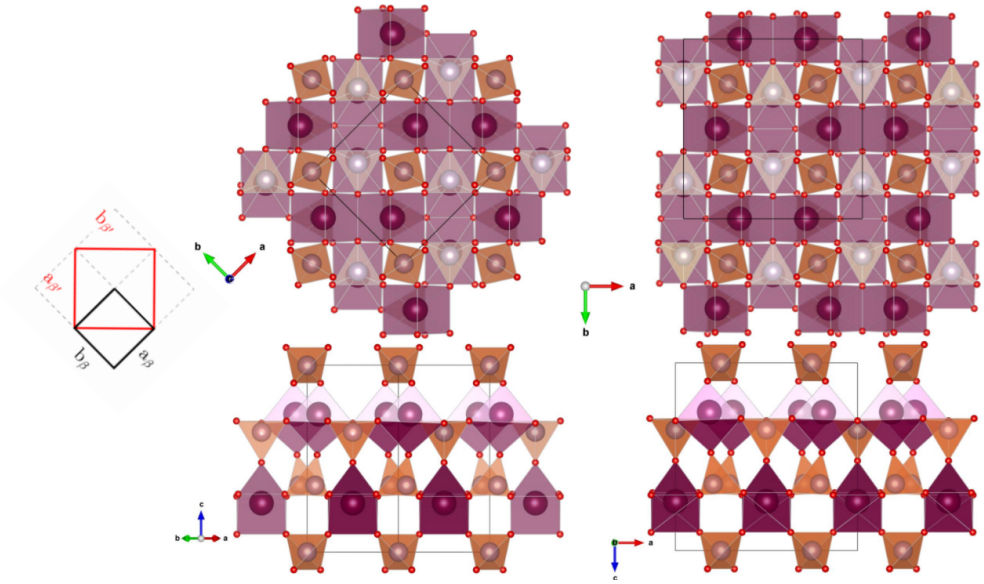

Figure 4: Projections of the β (left) and β' (right) phase structures. Top: view along the c axis. Bottom: view along the face diagonal ab for the paraelectric (β) phase and perpendicular to a for the ferroelectric (β') phase, illustrating their structural equivalence.

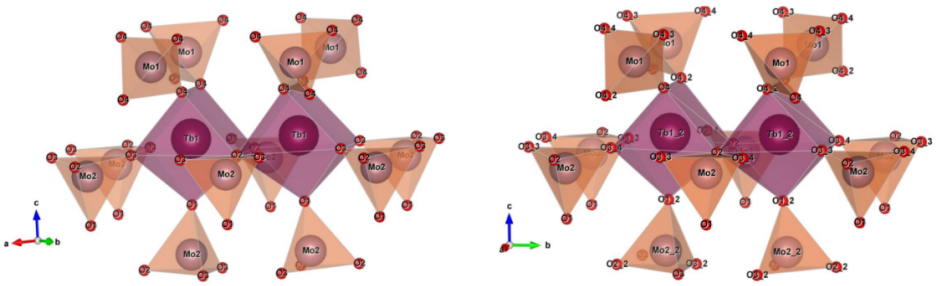

Figure 5: Coordination environments of the two Tb sites in the β (left) and β' (right) phases. The types of oxygen forming each tetrahedron are shown; in the ferroelectric phase (β'), the Tb_1–O_1 environment must be added, analogous to the $Tb_{1,2}$–O_2 environment.

1.5.2 Structure of the β' Phase: Induced Distortion and Improper Ferroelectricity

Upon cooling, the system undergoes a structural transition to the β' phase, which crystallizes in the orthorhombic system, space group *Pba2* (No. 32), with $Z = 4$, and whose c axis becomes polar. This symmetry reduction effectively doubles the unit cell, described by the basis transformation:

$$\begin{pmatrix} \vec{a}' \\ \vec{b}' \\ \vec{c}' \end{pmatrix} = \underbrace{\begin{pmatrix} 0 & -1 & 0 \\ 1 & 1 & 0 \\ 0 & 0 & 1 \end{pmatrix}}_{A} \begin{pmatrix} \vec{a} \\ \vec{b} \\ \vec{c} \end{pmatrix}, \quad \vec{t} = \begin{pmatrix} 0 \\ \frac{1}{2} \\ 0 \end{pmatrix} \tag{1.6}$$

where A is the transformation matrix and $\vec{t} = (0, \frac{1}{2}, 0)$ the associated shift.
In this phase, three independent Mo sites appear, all in general $4c$ positions, along with increased structural complexity featuring twelve distinct oxygen sites: two from O1, two from O2, four from O3, and four from O4. This proliferation of sites directly results from the loss of symmetry. The rare-earth atom (RE) now occupies two $4c$ sites, each coordinated by seven oxygens (see Figures 4 and 5).

Despite these differences, the overall connectivity is preserved: the more symmetric MoO_4 tetrahedra remain coordinated to four REO_7 polyhedra, while the less symmetric ones coordinate to five. The RE coordination polyhedra still share an edge and are surrounded by seven molybdate tetrahedra, enabled by the translational symmetry associated with the a and b glide planes and the polar axis parallel to c.

1.5.3 Group–Subgroup Relations and Structural Distortions

From a symmetry standpoint, the orthorhombic space group *Pba2* is a subgroup of the tetragonal group $P\bar{4}2_1m$, which allows the structural transition between these two phases to be described via group–subgroup theory. However, this relation is neither *translationengleich* nor *klassengleich*, since the transition loses both part of the point-symmetry (from $4mm$ to $mm2$) and certain translations, due to the change from a tetragonal to an orthorhombic lattice. Therefore, it is a *general* or *reductive* subgroup, in which the reduction involves transformations in both point symmetry and the translation lattice. This transformation entails two fundamental effects:

- A spontaneous strain of the crystal system (tetragonal to orthorhombic), which gives rise to ferroelasticity.
- A secondary polar distortion, responsible for the emergence of spontaneous polarization along the c axis, resulting in the improper ferroelectric character of the β' phase.

Analysis via *amplimodes* allows this transition to be decomposed into global distortion modes of the high-symmetry group. Three main types are identified[29]:

1. **Primary nonpolar mode**, with symmetry $M_2^+ \oplus M_4$, associated with the $M = (1/2, 1/2, 0)$ point of the Brillouin zone. This mode breaks the tetragonal symmetry and directly generates the orthorhombic structure observed in space group *Pba2*.
2. **Secondary polar mode**, with symmetry Γ_3, centered at the Γ point. It is not unstable by itself in the paraelectric phase, but its appearance is induced by coupling with the primary mode. This mode lowers the symmetry only to the intermediate subgroup $Cmm2$ and is responsible for the spontaneous polarization.
3. **Mode** Γ_1, symmetric, which does not break the original symmetry but acts as an additional compatible contribution.

The symmetry subspaces associated with these distortions have dimensions of 22 ($M_2^+ \oplus M_4$), 15 (Γ_3), and 14 (Γ_1), respectively—totaling 51 independent parameters, in agreement with the number of free positional coordinates in the conventional description of the *Pba2* structure.

A quantitative analysis shows that the primary mode $M_2^+ \oplus M_4$ dominates the total distortion, with an amplitude more than an order of magnitude larger than that of the secondary polar mode Γ_3 and the Γ_1 mode. The Γ_3 mode mainly involves atomic displacements in the xy plane, whereas the displacements along z—the only polar direction—are much smaller. In fact, given the very small amplitude of the Γ_3 distortion, its z-displacements (except for Mo atoms) are practically zero within experimental error. Jeitschko[23] already noted that the estimated value of spontaneous polarization in this structure, assuming nominal charges, was smaller than its standard deviation.

This mechanism confirms that ferroelectricity in $RE_2(MoO_4)_3$ compounds is improper, according to the definition of Toledano & Toledano[22]: the polar distortion is not the primary driver of the transition, but a consequence of coupling to an unstable nonpolar mode. Hence, the resulting spontaneous polarization magnitude is much lower than in proper ferroelectrics, although structurally significant.

2 Methodology I: Experimental Conditions

Chapter 2 Summary

Before addressing the analysis and refinement of the diffraction patterns of the Dy, Ho and Tb trimolybdates, which form the core of this work, this chapter provides a general description of the experimental protocols and methodologies used to obtain the data. Although the focus of the Final Degree Project lies in the treatment and analysis of the results, it is essential to understand the origin of the data. For this reason, the solid-state synthesis conditions of the ferroelectric β' phase of $RE_2(MoO_4)_3$ are described, including grinding, compaction and calcination steps. The theoretical basis of the DFT calculations performed with VASP for the β and β' phases of terbium molybdate is also briefly outlined. The chapter specifies the experiment carried out at the Institut Laue–Langevin (ILL), and explains the basic principles of neutron and X-ray generation, as well as their interaction with matter through scattering and absorption. The main features of the powder diffractometers used, D2B at ILL and X'Pert PRO at CAI–UCM, are also described, highlighting their advantages and limitations in the context of these compounds. Finally, the specific experimental conditions of the measurements are given, justifying their choice and emphasizing their role in obtaining the high-quality data on which this study is based.

2.1 Starting Point

2.1.1 Synthesis of the Molybdates

Rare-earth molybdates are commonly synthesized via solid-state reactions, in which precursor oxides (RE_2O_3 and MoO_3) are mixed and subjected to high-temperature heat treatments. The resulting phases depend not only on stoichiometry but also on processing parameters such as heating rate, sintering temperature, compaction pressure, and reaction time.

The CCDD research team (Crecimiento, Caracterización y Difracción de Materiales Dieléctricos) at the University of La Laguna has extensive experience in synthesizing these compounds, whose main challenge lies in obtaining phase-pure materials. In this work, we aimed to synthesize the ferroelectric β'-$RE_2(MoO_4)_3$ phase while avoiding the formation of its polymorphs: the modulated cheelite α phase and the negative-thermal-expansion γ phase.

In particular, the β' and γ phases of holmium trimolybdate are obtained by distinct heat treatments: 1173 K for 24 h for the β' phase and 1250 K for 48 h for the γ phase[32]. For terbium trimolybdate, starting from Tb_4O_7 and MoO_3, the α phase forms at 973 K and the β' phase at 1223 K[30]. The β' phase of dysprosium molybdate was synthesized under the same conditions as holmium; no prior CCDD publications exist for this compound.

Although the syntheses were not performed directly in this work, rare-earth molybdates are obtained by solid-state reaction—following protocols detailed in Eva González Correa's TFG[35]. In brief, precursor oxides are weighed precisely on a Sartorius ED 1245 balance, ground in an agate mortar (ICL 13 mm die), compacted in an Atlas–15 T hydraulic press, and finally calcined in Carbolite STF 12/300 and STF 15/180 furnaces (Fig. 6). This setup ensures homogeneous grinding, uniform compaction, and reproducible calcination—key for obtaining monophase $RE_2(MoO_4)_3$.

Figure 6: Equipment used for solid-state synthesis: (a) Sartorius ED 1245 balance, (b) disassembled 13 mm agate mortar (ICL), (c–d) assembled mortar, (e) Atlas–15 T hydraulic press, (f) Carbolite STF 12/300 furnace, and (g) Carbolite STF 15/180 furnace. From Eva González Correa[35].

2.1.2 Theoretical Calculations

Density Functional Theory (DFT) is a widely used *ab initio* method in quantum chemistry and solid-state physics for describing many-electron systems. Its main advantage is the ability to compute electronic properties at relatively low computational cost compared to more accurate but expensive quantum methods.

The ELSimMat research group (Electronic Structure and *ab initio* Simulations of Materials) at the University of La Laguna has a long record in theoretical studies of crystal structure, electronic properties, and phonons in various materials (e.g.,[36]), sometimes in collaboration with CCDD[37].

In this work, we used the computed crystal structures of the β and β' phases of terbium molybdate ($Tb_2(MoO_4)_3$)[30]. Calculations were performed with VASP[38], using DFT with pseudopotentials and plane-wave basis. For each volume, a full optimization of atomic positions and lattice parameters was carried out, constrained by the initial space-group symmetry (phases β and β') and the corresponding Wyckoff positions.

2.1.3 Proposal and Experiment at Large-Scale Facilities

As part of the study of rare-earth molybdates with ferroelectric, ferroelastic, and negative-thermal-expansion properties, experiments at large-scale facilities have been conducted to precisely characterize the crystal-structure evolution under pressure and temperature, as well as phase transitions. These studies are essential to correlate crystal structure with observed nonlinear properties, particularly in compounds with the β' phase of $RE_2(MoO_4)_3$. Complementary techniques—X-ray and neutron diffraction—enable a more complete structural characterization.

Within this context, the CCDD group participated in an experimental campaign on the D2B neutron diffractometer (proposal **[47488]**) at the Institut Laue-Langevin (ILL)[39] in Grenoble, France (Fig. 7).

Polycrystalline samples of $Ho_2(MoO_4)_3$, $Dy_2(MoO_4)_3$, and $Tb_2(MoO_4)_3$ were studied by neutron diffraction at multiple temperatures (225–475 K), complemented by X-ray powder diffraction at the Complutense University of Madrid (CAI-XRD) using a conventional powder diffractometer[40]. The experimental data serve as the basis for the structural analyses and their temperature evolution presented in this work.

Figure 7: Institut Laue-Langevin (ILL).

Between 1993 and 1995, the ILL reactor was refurbished to deliver the world's highest continuous neutron flux in the moderator region—1.5×10^{15} n·s^{-1}·cm^{-2} at 58.3 MW thermal power. It operates in cycles of 50 days followed by refueling stops, plus an annual long maintenance shutdown, for a total of 200 days of science per year.

The reactor's main role is to produce an intense neutron flux for cutting-edge research. These neutrons, extracted, collimated, and directed to experimental stations, are used to study materials, analyze molecular structures, and explore fundamental physical processes.

2.2 Neutron and X-ray Diffraction

2.2.1 Generation of Neutrons and X-rays

Structural studies by diffraction techniques require radiation sources that interact effectively with the atoms in the crystal. In this work we employed two complementary types of radiation: thermal neutrons, generated in a research nuclear reactor, and X-rays, produced in a conventional powder diffractometer with a copper anode tube. Both radiations yield structural information but interact differently with matter: X-rays scatter from the electron cloud, making them more sensitive to heavy atoms, whereas neutrons scatter from the nucleus, providing higher sensitivity to light atoms such as oxygen.

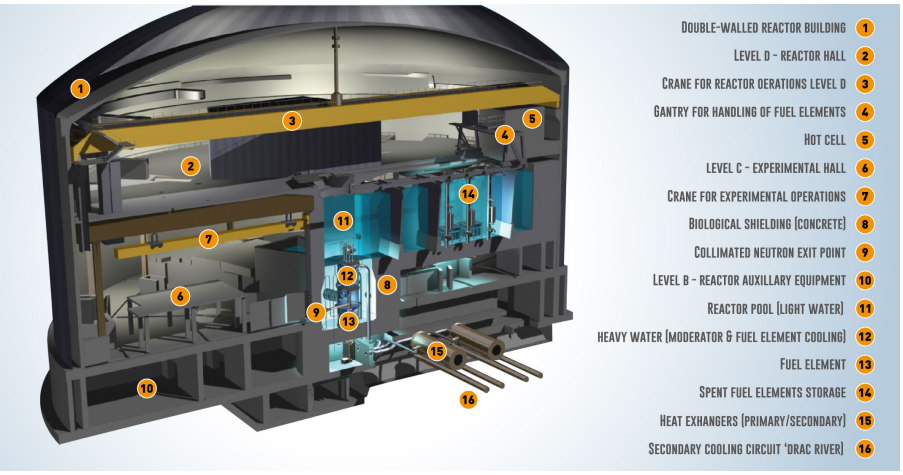

Figure 8: ILL nuclear reactor and its components[41]

Thermal Neutrons: Reactor Generation and Characteristics

Unlike spallation sources, where neutrons originate by bombarding a heavy-metal target with accelerated protons, the process in the ILL reactor (Fig. 8) begins with neutron generation in the core (13), where ^{235}U undergoes fission upon absorbing thermal neutrons.

These initial neutrons are provided by external sources installed at reactor start-up. A common source is an ^{241}Am–^{9}Be combination: alpha particles from ^{241}Am react with Be to produce ^{12}C and free neutrons via:

$$\alpha + {}^{9}\mathrm{Be} \rightarrow {}^{12}\mathrm{C} + n \tag{2.1}$$

These neutrons initiate the first fission reactions in the fuel. Once fission begins, more neutrons are released, establishing a self-sustaining chain reaction. From that point on, the reactor operates without the need for external sources. The secondary neutrons are moderated with heavy water (D_2O), allowing efficient control of the reaction (12). Simultaneously, the core is cooled with light water contained in the reactor pool (11). The radiation generated is contained by a biological concrete shield (8).

The useful neutrons are extracted through collimated channels (9) toward experimental laboratories (6), where they are used for advanced studies of materials and molecular structures. The residual heat is transferred via heat exchangers (15) to a secondary circuit (16), which uses water from the Drac River for dissipation. Finally, the spent fuel is moved to the storage area (14), where radioactive waste is safely managed.

The neutrons used for crystal diffraction are slowed down through successive collisions with the moderator until they reach thermal equilibrium with the surroundings. These thermal neutrons then exhibit a velocity distribution that follows the Maxwell–Boltzmann statistics at the moderator temperature ($T \approx 300$ K).

The average energy of these thermal neutrons is on the order of 25 meV, corresponding to a typical velocity of approximately 2200 m/s.

By De Broglie's relation:

$$\lambda = \frac{h}{m\,v} \tag{2.2}$$

where h is Planck's constant, m the neutron mass, and v its velocity, typical wavelengths of 1.5 to 1.8 Å are obtained, comparable to interatomic distances in crystalline solids. These wavelengths make thermal neutrons ideal for diffraction studies, as they satisfy Bragg's law for atomic planes with spacings on the order of 1–5 Å. At the ILL, once moderated, the neutrons are guided through neutron guides to the experimental instruments (Figure 9).

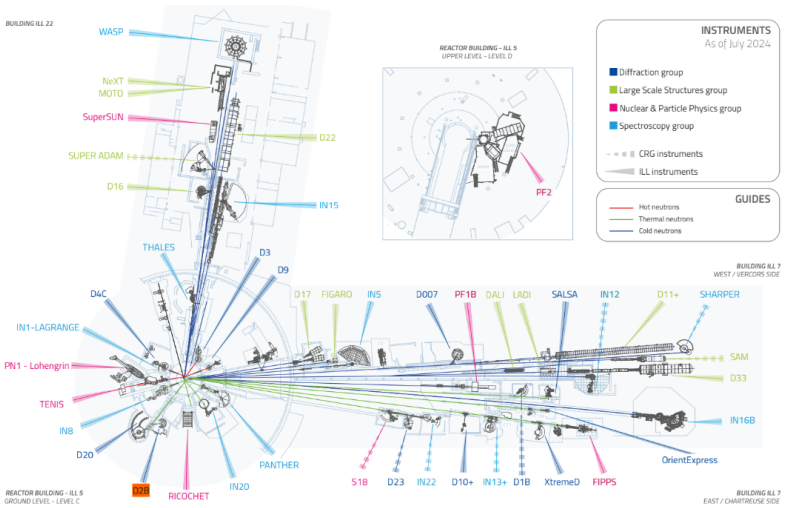

Figure 9: ILL experimental stations[39]. We focus on the D2B powder diffractometer (orange box).

After their production, thermal neutrons must be efficiently transported to the experimental instruments. This is accomplished using neutron guides, which rely on total internal reflection at very small glancing angles. Such guides are coated with special reflective materials that allow neutrons to be conveyed over long distances (tens to hundreds of meters) without significant loss of flux.

X-rays: Generation in a Copper Anode Tube

The X-ray radiation used in conventional powder diffractometers is generated by an X-ray tube with a copper anode. The CAI also has other types of tubes for different investigations. In this device, electrons are emitted from a heated filament and accelerated by a high voltage difference (30–45 kV) until they strike the copper anode (Figure 10). This collision excites the metal's inner electrons, and when these vacancies are filled by electrons from higher energy levels, characteristic radiation of the material is emitted.

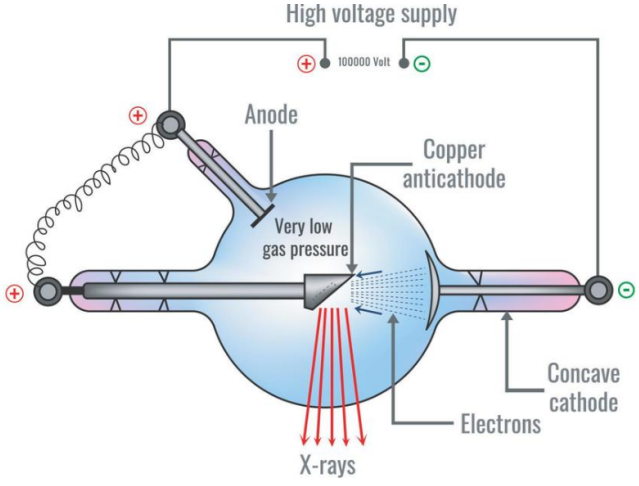

Figure 10: Schematic of a copper-anode X-ray tube[42]

The Cu Kα line, with a wavelength of $\lambda = 1.5406$ Å, is the most commonly used in powder diffraction, as its value is optimal for studying typical interatomic distances and ensures that diffraction angles (2θ) fall within an easily accessible range (5°–90°). Much shorter wavelengths (such as Mo Kα, $\lambda = 0.7107$ Å) would require very small diffraction angles and reduce angular resolution, while longer wavelengths would cause peak overlap and increased absorption.

Therefore, Cu Kα radiation represents an ideal compromise between resolution, angular coverage, and detection efficiency. The radiation is carefully collimated and filtered to eliminate other lines (such as Kβ) and to maximize spectral purity.

2.2.2 Radiation–Matter Interaction

Unlike X-rays, which scatter from the electronic clouds of atoms, neutrons interact primarily with atomic nuclei and, thanks to their magnetic moment, also with the magnetic moments of electrons. This dual sensitivity makes neutrons a complementary probe to X-rays for studying both atomic and magnetic structures of materials[43].

Depending on the interaction mechanism between neutrons or X-rays and matter, two main phenomena are distinguished: scattering and absorption. In the case of X-rays, photons are scattered by electrons—especially those in outer shells—whereas neutrons are deflected by strong nuclear forces upon interacting with nuclei.

In absorption, the mechanisms also differ: in photoelectric absorption, photons are captured by inner-shell electrons (K or L shells), which may lead to emission of characteristic X-rays or Auger electrons[44]. In neutron absorption, neutrons may be captured by the nucleus, inducing gamma-ray emission or even nuclear reactions such as fission or activation. Both scattering and absorption cross-sections quantify these interactions, expressing the probability of an incident particle interacting with an atom or nucleus in barns (1 barn = 10^{-28} m^2)[45].

For neutron scattering, one often uses the coherent scattering length b_{coh}, measured in femtometers (1 fm = 10^{-15} m). This length characterizes the wave amplitude scattered by a nucleus and relates directly to the scattering cross-section, distinguishing coherent from incoherent scattering[46].

In X-ray scattering, intensity depends on atomic number Z: higher Z yields stronger scattering. The analogous quantity is the atomic form factor $f(\theta)$[32], which describes the efficiency of a bound electron scattering as a function of angle. It decreases with increasing 2θ, reducing sensitivity to precise atomic positions at high angles and lowering contrast between light and heavy atoms. In contrast, neutron scattering does not scale with Z, since it involves nuclear forces; scattering amplitudes vary irregularly across isotopes.

For example, oxygen (Z = 8) has a $b_{\text{coh}} \approx 5.803$fm, comparable to that of molybdenum (Mo, $b_{\text{coh}} \approx 6.715$fm), which enables the precise localization of light atoms in neutron diffraction. Both O and Mo exhibit low incoherent scattering, favoring high-quality data. Moreover, this technique allows for distinguishing between isotopes and between consecutive elements in Z, as observed in the case of hydrogen and deuterium. Additionally, the lack of dependence on the scattering angle means that no diffracted intensity is lost at high angles, which is advantageous for determining the atomic and thermal parameters of the crystal structure. For both types of radiation, a distinction is made between elastic and inelastic scattering. When X-rays or neutrons are scattered without energy change, only altering their direction, this is referred to as elastic scattering, which gives rise to diffraction patterns.

Inelastic scattering, on the other hand, involves an exchange of energy, allowing the study of excitations such as phonons or magnons when neutrons interact. In the case of X-rays, Compton scattering is the inelastic process that occurs, where photons lose energy upon interacting with electrons; it does not produce diffraction peaks but contributes to the background of the pattern, especially when detectors do not discriminate in energy[47]. For neutrons, coherent elastic scattering refers to the case in which the scattered waves interfere constructively, generating diffraction peaks and revealing the crystalline order.

Moreover, thanks to the magnetic moment of neutrons (spin = 1/2), they can interact with the magnetic moments of atoms, making it possible to study magnetic structures through spin-dependent coherent scattering, as in ferromagnets or antiferromagnets. In contrast, incoherent elastic scattering results from random interactions without phase correlation between the scattered neutrons, producing a diffuse background. This occurs due to two main factors[48]:

1. Variability between isotopes: Different isotopes of the same element can have very different scattering cross sections, even with opposite signs (e.g., Gd-155: −81.3fm; Gd-157: +90fm).

2. Nuclear spin disorder: If nuclei have multiple spin states, as in hydrogen (^{1}H), neutrons are scattered with random phases, resulting in very high incoherent scattering ($\sim$ 80 barns). In contrast, deuterium (^{2}H) has much lower incoherent scattering ($\sim$ 2 barns), which reduces the diffuse background and improves structural resolution.

Inelastic neutron scattering can also be either coherent (collective phonons) or incoherent (local excitations). Coherent scattering provides access to the collective dynamics of the lattice, whereas incoherent scattering reveals local processes and contributes to the spectral background. As for absorption, it varies drastically between elements and isotopes for neutrons due to nuclear resonances. Each nucleus has discrete energy levels, and if a neutron forms a compound state with the nucleus, a resonance absorption can occur, producing extremely large cross-section peaks at specific energies.

Elements such as ^{10}B, ^{113}Cd, ^{157}Gd, or ^{149}Sm exhibit extremely high absorption cross sections (for example, Gd $\approx$ 49,000 barns). Furthermore, many absorptions follow the inverse velocity law ($\sigma \propto 1/v$), which implies greater absorption at lower energies (thermal neutrons). For instance, ^{1}H has an absorption cross section of 0.332 barns, whereas ^{2}H has only 0.000519 barns. This justifies the use of deuteration in neutron diffraction experiments to reduce intensity losses and improve signal quality[49].

Finally, we justify why we did not select trimolybdates with Gd, Eu, or Sm. Although β'-$Gd_2(MoO_4)_3$ is the first known ferroelectric of this family, it presents serious challenges for neutron diffraction: its extremely high absorption (49,000 barns) reduces detected intensity and introduces errors. Moreover, Gd's nuclear scattering is highly anomalous and varies significantly between isotopes, introducing incoherent noise. Sm (5920 barns) and Eu (4530 barns) also absorb strongly. In general, these elements degrade the quality of diffraction data, reduce resolution, and raise the background, hindering structural refinement[49]. For these reasons, we opted for compositions free of these elements in our study.

As a summary and culmination of the aspects discussed regarding radiation–matter interaction, we can express how diffracted intensity is quantified in an experiment, both for X-rays and neutrons. Although the interaction mechanisms differ—electrons versus nuclei—the formal treatment of crystal diffraction retains an analogous mathematical structure.

In the case of X-ray diffraction, the observed intensity for a diffraction peak hkl is proportional to the square modulus of the structure factor F_{hkl}, corrected by geometric and experimental factors:

$$I_{hkl}(\mathrm{X}) \propto |F_{hkl}(\mathrm{X})|^2 \, L(\theta) \, P(\theta) \, A(\theta) \tag{2.3}$$

Where $F_{hkl}(X) = \sum_j f_j(\theta) \, e^{2\pi i(hx_j+ky_j+lz_j)}$ is the structure factor (with $f_j(\theta)$ the atomic form factor of atom j); $L(\theta)$ is the Lorentz factor; $P(\theta)$ is the polarization factor; and $A(\theta)$ is the absorption correction.

For neutron diffraction, the formula is analogous, but $f_j(\theta)$ is replaced by the coherent scattering length b_j:

$$I_{hkl}(n) \propto |F_{hkl}(n)|^2 \, L(\theta) \, A(\theta) \tag{2.4}$$

Where $F_{hkl}(n) = \sum_j b_j \, e^{2\pi i(hx_j+ky_j+lz_j)}$ is the neutron structure factor (with b_j the nuclear scattering length of atom j); $L(\theta)$ is the Lorentz factor; and $A(\theta)$ the absorption correction.

Unlike X-rays, neutrons do not have a polarization factor, since they are non-electromagnetic particles. However, in experiments using polarized neutrons, additional terms associated with magnetic interaction may appear.

These expressions quantitatively summarize how diffraction peak intensities are generated and modulated, and they help to understand how the fundamental differences between X-ray and neutron interactions with matter translate into advantages and limitations depending on the type of structural or magnetic study to be conducted.

2.2.3 Powder Diffraction

Powder diffraction is an essential technique in crystallography for analyzing polycrystalline or powdered materials. Unlike single-crystal diffraction, which relies on a single, well-oriented crystal, powder diffraction uses a sample composed of many microcrystals randomly oriented, ensuring that all possible lattice plane orientations are present.

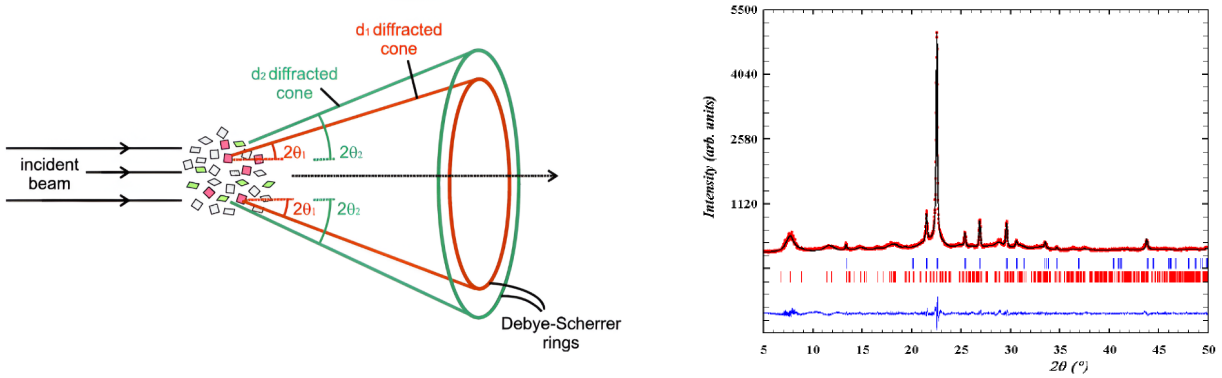

Figure 11: (Left) Formation of diffraction cones in powder diffraction experiments from planes (hkl) satisfying Bragg's law[50]. These cones produce rings (Debye–Scherrer rings) or bands on the detector, depending on geometry, which allow calculation of interplanar spacings d_{hkl}. The diffraction angles θ_1 and θ_2 are indicated. (Right) Typical powder pattern obtained with FullProf.

As a result, the incident radiation can satisfy the Bragg condition for many families of planes simultaneously. For each family of planes with an interplanar spacing d_{hkl}, a diffraction cone is formed with an opening angle of 4θ, where 2θ is the diffraction angle between the incident and diffracted beams (see Figure 11, Left).

These cones intersect the detector as concentric rings when using an area detector, or as bands when using a curved "banana"-type detector, commonly employed in neutron diffraction (such as in the D2B instrument at ILL). By measuring the radius or angular position of these rings or bands, the angle θ can be determined, and the interplanar distances d_{hkl} calculated using Bragg's law.

The diffractogram is the graphical representation of a powder diffraction experiment, showing the intensity of diffracted radiation as a function of the angle 2θ. The peaks in the diffractogram —their angular positions and intensities— contain key information: they allow identification of the crystalline phases present in the sample, estimation of lattice parameters, and assessment of microstructural properties such as crystallite size, texture, and possible internal stresses (see Figure 11, Right).

Neutron Powder Diffractometer

The D2B neutron powder diffractometer at the Institut Laue–Langevin (ILL) (see Figure 12) is a high-resolution instrument for structural studies. Widely used for polycrystalline materials, it features exceptional angular resolution. Its optimized design records diffraction peaks precisely while minimizing noise, facilitating complex structure refinements.

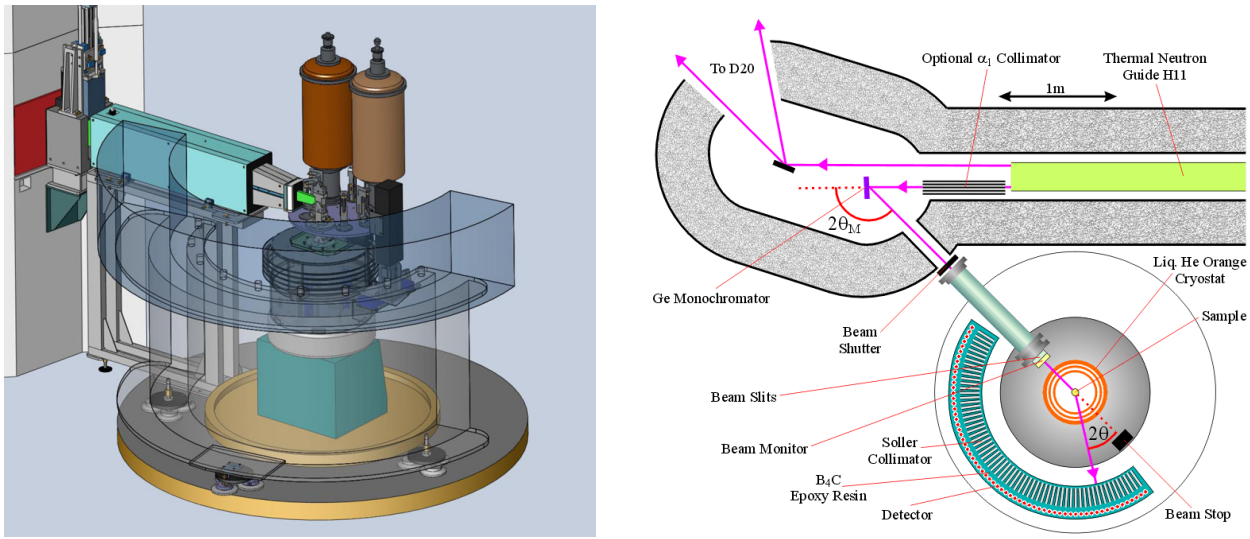

Figure 12: 3D layout (left) and internal structure/function (right) of the ILL D2B diffractometer [51].

A typical neutron powder diffractometer consists of a neutron source (a high-flux research reactor). A germanium (Ge[335]) single-crystal monochromator selects neutrons of precise wavelength (λ = 1.5943 Å) by Bragg reflection. A collimation system shapes the neutron beam geometry to optimize measurements (Fig. 12). The sample is contained in an aluminum tube (approximately 5–10 mm in diameter, 0.1–1 ml volume), mounted on a rotating stage. The D2B's chief advantage lies in its array of 128 fixed ^{3}He-filled detectors (300 mm tall), which simultaneously cover a wide angular range (0–160°) without detector movement. The take-off angle (between the incident beam and the detector center) was 135°, and a full diffraction pattern was recorded in 100 increments of 0.025° in 2θ. From the raw data, two patterns were extracted: one by binning pixels in the detector's central equatorial region (highest angular resolution, sharper peaks), and another integrating all detectors (better counting statistics, lower resolution).

For thermodiffraction, the D2B (Fig. 12) is equipped with high-temperature furnaces, enabling measurements under extreme temperature and pressure without compromising data quality. These capabilities make the D2B one of the most advanced neutron powder diffractometers available. In our study, diffraction patterns were collected at 225, 275, 300, 375, 425, and 475 K, each over approximately 2.5 h (totaling three days of beam time). The transmission geometry with sample rotation minimizes preferred orientation of microcrystals and yields more homogeneous absorption, ideal for structural refinement. Neutron diffraction requires larger sample volumes than X-ray diffraction, but neutrons' high penetration leads to reduced interactions with sample environments and less influence from external materials, offering greater stability for non-ambient studies.

X-ray Powder Diffractometer

A conventional PANalytical X'Pert PRO powder diffractometer was used (Fig. 13) in Bragg–Brentano (reflection) geometry at the CAI X-Ray Diffraction Service, Universidad Complutense de Madrid. This instrument is built around a vertical θ–2θ goniometer (sample always horizontal) with a Cu Kα X-ray tube and interchangeable sample stages optimized for thermodiffraction.

The incident beam optics consisted of a programmable divergence slit, operable in fixed-divergence or fixed-irradiated-length modes (0.5° in our experiments), plus an anti-scatter slit (1° in our experiments). The diffracted beam was detected by a fast X'Celerator detector with an optional flat secondary monochromator for Cu Kα_1, eliminating Cu Kα_2 radiation and yielding $\lambda = 1.5405(1)$ Å (Cu Kα_1).

A Soller slit was installed in front of the detector to reduce low-angle peak asymmetry. The available sample stages allow rotation; we used a 14×10 mm^2 holder. With the X-ray tube fixed, the sample rotates by θ and the detector by 2θ, ensuring the incident and diffracted beam both form angle θ with the reflecting planes, as required by Bragg's law. Our scan range was $10° < 2\theta < 100°$, continuous at 0.02° steps with 200 s per step.

For thermodiffraction, an Anton Paar TTK 450 high-temperature chamber was used. Measurements were taken at 225, 275, 300, 375, 425, and 475 K during cooling under 5×10^{-4} mbar vacuum, at 10 K/min with a 5-minute dwell between points to stabilize the sample temperature. Reflection geometry has disadvantages versus transmission: surface illumination, more critical absorption, preferred orientation (powder texture), and microabsorption due to grain size/density variations. These effects are difficult to correct without appropriate models: they do not affect cell parameters but can compromise atomic position refinement if uncorrected.

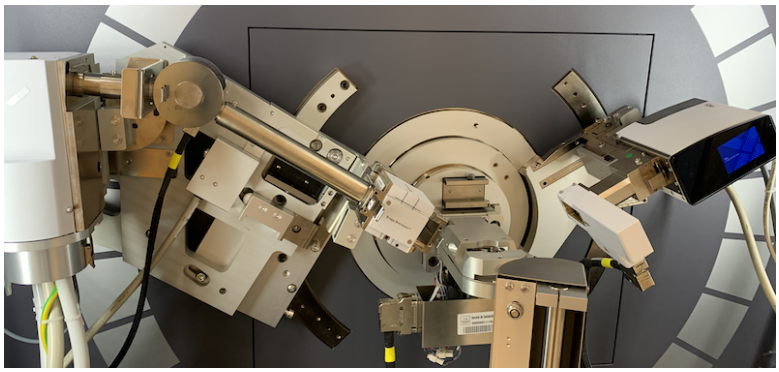

Figure 13: CAI-UCM PANalytical X'Pert PRO powder diffractometer[40].

3 Methodology II: Rietveld Refinement

Chapter 3 Summary

The structural refinement carried out in this work, mainly using `FullProf`*, constitutes one of the most important parts of the project and required a substantial amount of time and effort. Rietveld refinement was applied to neutron diffraction patterns, while the X-ray diffraction data were treated using the Le Bail method, since the experimental quality and structural defects did not allow a robust full Rietveld refinement in that case. A multiphase and multipattern model was built to refine key parameters such as lattice constants, atomic positions, crystallite size, microstrain and instrumental effects. The peak profiles were described using the Thompson–Cox–Hastings pseudo-Voigt function, with parameters associated with broadening and asymmetry adapted to the characteristics of each pattern. The background was modelled using Taylor polynomials for neutron diffraction and Chebyshev polynomials for X-ray diffraction. In addition, the neutron diffraction data were treated through advanced amplimode-based refinement, using tools from the Bilbao Crystallographic Server and* `FullProf` *to describe the structural distortions as symmetry-adapted collective modes. This methodology reduces the number of refined parameters, improves the physical interpretation of the phase transition and allows comparison of the evolution of distortion modes in the Tb, Dy and Ho molybdates as a function of temperature, hydrostatic pressure and chemical pressure.*

For the structural study of the general-formula compound $RE_2(MoO_4)_3$ (where RE is a rare-earth element), we employed the Rietveld method, which requires theoretical models. Our initial structural models derive both from *ab initio* calculations and from Crystallographic Information Files (CIFs) available in the Inorganic Crystal Structure Database (ICSD)[52]. ICSD is an internationally recognized repository of experimentally determined crystal structures published in the scientific literature. Each CIF contains all necessary information to describe a crystal structure—cell parameters, atomic positions, occupancy factors, and thermal parameters—making it an ideal starting point for structural refinements. From these models, theoretical diffraction patterns can be generated using the `FullProf` program[53], which simulates diffraction profiles from defined crystal structures. Comparing these simulated patterns with the experimental data allows us to evaluate the suitability of the initial model. The closer the agreement between simulated and observed patterns, the more robust the starting point for the Rietveld refinement, facilitating faster and more accurate convergence of the fit and reliable extraction of structural parameters such as lattice constants, atomic positions, and occupancy factors.

3.1 Introduction to Refinement

The Rietveld method[54] is a structural analysis technique that provides detailed information about a material's crystal structure from its diffraction pattern (whether X-ray or neutron). Its basis is fitting a theoretical model to the experimental data using a least-squares approach, minimizing the difference between observed and calculated intensities at each point in the diffraction profile. This difference is quantified by a residual function S_y, which depends on all structural, microstructural, and instrumental parameters contributing to the diffraction pattern:

$$S_y = \sum_i w_i \left(y_i^{\text{obs}} - y_i^{\text{calc}}\right)^2 \tag{3.1}$$

The goal of the refinement is to find the optimal set of parameters that minimizes S_y.

In the case of neutron diffraction, this technique is especially valuable for complex materials such as rare-earth molybdates $RE_2(MoO_4)_3$ (with RE = Tb, Ho, Dy), due to its sensitivity to light elements like oxygen and its ability to distinguish neighboring elements in the periodic table. The theoretical model used in the refinement includes fundamental aspects such as the space group, the crystal structure, and the atomic positions within the unit cell. It also incorporates microstructural parameters like crystallite size, microstrain, and phase fractions. Additionally, instrumental effects are considered, including peak broadening due to the instrument's optics.

The FullProf program[53] was used for the refinement. A multi-phase, multi-pattern model was constructed with shared parameters across phases to reduce the degrees of freedom in the fit.

In each instruction file (`.pcr`), seven phases were refined simultaneously: the three rare-earth molybdate phases (Tb, Dy, and Ho), an aluminum phase, and three additional phases used for Le Bail refinement. A total of nine diffraction patterns were used: six neutron patterns and three X-ray patterns (one of each technique for each molybdate). For the neutron data, both the full detector patterns and the patterns centered on the detector's central region were considered. The calculated intensity at each point $Y_{i,c}$ is obtained by summing the contributions of all phases present in the sample. Each contribution depends on several factors:

$$Y_{i,c} \;=\; \sum_j Y_{i,j} \;=\; \sum_j S_j \sum_K L_{K,j}\, F^2_{K,j}\, \phi_{K,j}\big(2\theta_i - 2\theta_{K,j}\big)\, P_{K,j}\, A \;+\; y_{b,i} \tag{3.2}$$

Where:

- S_j is the scale factor adjusting the overall intensity of each phase.
- K_j denotes the Bragg reflection for a given set of Miller indices.
- $L_{K,j}$ are correction factors such as Lorentz, polarization, and multiplicity, refined for each phase except in Le Bail refinements.
- $F^2_{K,j}$ is the structure factor squared, dependent on atomic positions and thermal parameters, refined separately for each phase.
- $\phi_{K,j}$ is the peak profile function, centered at the Bragg angle $2\theta_K$, and depends on cell parameters (kept identical across patterns for a given phase).
- $P_{K,j}$ and A represent any additional profile and absorption corrections.
- $y_{b,i}$ is the background intensity at point i.

3.2 Modeling of the Diffraction Peak Profile in Rietveld Refinement

Accurate modeling of the diffraction peak profile is crucial to obtain reliable structural and microstructural parameters in a Rietveld refinement. The most widely used function to describe each peak profile is the *Thompson–Cox–Hastings* (TCH) function[55], which offers a computationally efficient approximation to the Voigt convolution and can represent both instrumental and microstructural broadening. The TCH function models the profile as a weighted sum of Gaussian and Lorentzian contributions via a pseudo-Voigt:

$$pV(x) = \eta\, L(x) + (1-\eta)\, G(x) \tag{3.3}$$

where η is the mixing parameter (0 = purely Gaussian, 1 = purely Lorentzian), $L(x)$ and $G(x)$ are the Lorentzian and Gaussian functions, respectively, and $x = 2\theta - 2\theta_0$ is the angular deviation from the peak center $2\theta_0$. TCH extends this concept by introducing adjustable parameters to model peak asymmetry, commonly observed at low angles.

The Gaussian component, mainly due to instrumental effects, is given by:

$$G(x) = \frac{1}{HG\sqrt{\pi/\ln 2}}\, e^{-\frac{4\ln 2\, x^2}{HG^2}} \tag{3.4}$$

where HG is the FWHM of the Gaussian.

The Lorentzian component, related to microstructure (crystallite size and microstrain), is:

$$L(x) = \frac{1}{\pi}\, \frac{\frac{HL}{2}}{x^2 + \left(\frac{HL}{2}\right)^2} \tag{3.5}$$

where HL is the FWHM of the Lorentzian.

Both widths HG and HL vary with diffraction angle θ and are modeled by parameters reflecting instrument and microstructure. The Gaussian width squared is:

$$HG^2 = U\tan^2\theta + V\tan\theta + W \tag{3.6}$$

and the Lorentzian width:

$$HL = X\sec\theta + Y\tan\theta \tag{3.7}$$

These parameters have clear physical meanings:

- U, V, W: describe Gaussian instrumental broadening (beam divergence, geometry, resolution).
- X: associated with crystallite size broadening.
- Y: associated with microstrain broadening.

Often, the parameter U can also be related to microstrains and depends on temperature. The full width at half maximum (FWHM) of a peak is not simply the sum of HG and HL, but results from the convolution that combines both the Gaussian and Lorentzian components. The TCH function and its pseudo-Voigt approximation allow efficient modeling of this convolution, adjusting the relative weight via η.

In many diffraction patterns, especially at low angles, peaks show asymmetry, mainly due to axial divergence and other instrumental effects. The TCH function incorporates this asymmetry through two parameters: SL, which controls the slope or intensity of the asymmetric tail, and DL, which regulates its extent or decay rate.

For neutron diffraction, we used a well-characterized instrumental resolution function defined by the parameters U, V, and W. In our case, only the parameters U and Y were refined. The asymmetry was minimal or negligible, and therefore not refined.

In the refinement of X-ray diffraction data, we did not start from a perfectly defined instrumental function. Instead, we used initial values based on similar compounds and refined the parameters U, V, W, and X. Here, the parameter X plays a greater role, since crystallite size tends to have a stronger impact on the Lorentzian broadening in XRD. Axial divergence (asymmetry) is a predominant effect in X-rays, making SL and DL essential for accurate profile correction.

3.3 Background modeling in a diffraction pattern

In Rietveld refinement, a critical yet often underestimated aspect is the modeling of the background in the diffraction pattern.

This background represents the contribution from all intensities not arising from coherent Bragg diffraction and, therefore, not directly associated with the crystal structure of the sample.

Incorrect background modeling can distort the relative intensity of the peaks and compromise the reliability of the fit, affecting both structural and microstructural refined parameters. The background can have multiple physical origins.

In X-ray diffraction, it may include significant contributions from beam-induced fluorescence, especially if elements present in the sample strongly absorb the incident radiation. It may also originate from inelastic or Compton scattering, instrumental or electronic noise, or even the signal from the sample holder. In neutron diffraction, typical background sources include incoherent scattering, contributions from the experimental environment, and, generally, a lower proportion of fluorescence. A smooth background increase at high angles may also be observed, depending on the detection geometry or the type of source used.

Another relevant cause of background is the presence of amorphous or partially ordered material, such as a glassy phase, regions with local structural disorder, or weak superstructures.

These factors produce diffuse scattering, which may appear as a smooth modulation or broad, ill-defined structures in the baseline of the pattern. To effectively model this background, several strategies are available. One approach involves manually inputting a table of background intensities for specific 2θ values and then linearly interpolating between them. Although useful in some cases, this method is more prone to subjective errors and requires constant user input, making it less common in systematic refinements. We used it during the initial stages of the refinement.

More commonly, mathematical global functions are employed and refined simultaneously with the rest of the structural parameters, providing a continuous and reproducible description of the background over the entire angular range.

3.3.1 Taylor Polynomials

Among these functions, Taylor polynomials are widely used, especially in refinements of neutron diffraction data. These polynomials allow the background to be represented as a sum of terms of increasing order in 2θ, with coefficients refined during the fit.

Their versatility and ability to approximate a smooth curve make them ideal for patterns where the background shows a regular trend without large local fluctuations. In the case of neutrons, this approximation is particularly suitable because backgrounds tend to be smoother and more predictable, rising slowly toward high angles due to detector geometry and the shape of the neutron spectrum.

In our case, a third-order polynomial ($n = 3$; four coefficients) was sufficient to capture the general shape of the background without introducing too many additional parameters, which aids refinement stability. This function is expressed as:

$$Y_{b,i} = \sum_{m=0}^{n} B_m \Big(\frac{2\theta_i}{\mathrm{BKPOS}} - 1 \Big)^m \tag{3.8}$$

where $Y_{b,i}$ is the background intensity at point i; B_m are the polynomial coefficients (refinable parameters); $2\theta_i$ is the diffraction angle at point i; BKPOS is a scaling constant or the midpoint of the angular range; and n is the polynomial order (here $n = 3$).

3.3.2 Chebyshev Polynomials

In X-ray diffraction, we prefer the use of Chebyshev polynomials[56]. These functions, defined orthogonally on the interval $[-1, 1]$, allow a more controlled and stable mathematical representation of the background, especially when a larger number of terms is required to capture local modulations (due to physical phenomena such as fluorescence, disorder, or poorly crystallized phases) or complex curvature, particularly at low angles. To employ them, the diffraction angle axis (2θ) is rescaled to the normalized Chebyshev interval, enabling the direct use of their cosine-based expressions. The Chebyshev polynomials of the first kind are defined on $[-1, 1]$, and their general form in a refinement is:

$$Y_{b,i} = \sum_{m=0}^{n} C_m \, T_m(x_i) \tag{3.9}$$

where $Y_{b,i}$ is the background intensity at point i; C_m are the refinable coefficients; $T_m(x)$ are the Chebyshev polynomials of order m; and x_i is the rescaled angular variable, given by:

$$x_i = 2\,\frac{2\theta_i - 2\theta_{\min}}{2\theta_{\max} - 2\theta_{\min}} - 1 \tag{3.10}$$

to map $2\theta_i$ onto the interval $[-1, 1]$.

Chebyshev polynomials allow modeling these variations without introducing artificial oscillations that can distort the baseline when high-order Taylor polynomials are used. Moreover, their orthogonality provides a clear numerical advantage: many terms can be employed without degrading refinement stability or inducing unwanted correlations with other parameters. In our refinements, we used between 9 and 11 coefficients.

3.4 Treatment of Diffraction Intensities: Rietveld and Le Bail

3.4.1 Rietveld Refinement

In Rietveld refinement, the intensity of diffraction peaks is calculated from the structure factor, which represents the ability of a unit cell to scatter radiation coherently. This factor is determined by the nature and positions of the atoms within the cell, as well as by their scattering coefficient (in the case of X-rays) or scattering length (in the case of neutrons).

In a unified way, for a reflection hkl one has:

$$I_{hkl} \propto |F_{hkl}|^2 = \left| \sum_j p_j \, e^{2\pi i\,(hx_j + ky_j + lz_j)} \, e^{-B_j s^2} \right|^2 \tag{3.11}$$

Where:

$$p_j = \begin{cases} f_j(\theta), & \text{atomic scattering factor for X-rays,} \\ b_j, & \text{scattering length for neutrons,} \end{cases} \qquad s = \frac{\sin\theta}{\lambda}.$$

Here, (x_j, y_j, z_j) are the coordinates of atom j in the unit cell, and B_j is its thermal (Debye–Waller) factor.

3.4.2 Le Bail Refinement

This approach works robustly when high-quality diffractograms and well-defined structural models are available. However, in situations where data quality is limited—due to low angular resolution, poorly defined peaks, unknown phases, or preferred orientation—the direct fitting of observed intensities to calculated ones can lead to inconsistent or physically unrealistic results.

In such cases, the Le Bail method[54], introduced in 1988, provides an effective solution. This method allows full-profile refinement of the diffraction pattern without requiring knowledge of the atomic structure. Instead of calculating intensities from a structural model, they are treated as free parameters that are iteratively adjusted to reproduce the experimental profile. The only constraint is that the sum of the intensities of all reflections contributing to each point of the diffractogram matches the experimental signal minus the background.

The refinement proceeds iteratively. Starting from an initial estimate of the intensities $I_c^{(0)}(H)$, they are updated in each cycle $n+1$ according to:

$$I_c^{(n+1)}(H) = I_c^{(n)}(H) \;\cdot\; \frac{\sum_i \left[\frac{y_o(2\theta_i) - y_b(2\theta_i)}{y_c(2\theta_i)}\right] \phi\big(2\theta_i - 2\theta_H\big)}{\sum_i \phi^2\big(2\theta_i - 2\theta_H\big)} \tag{3.12}$$

Here, y_o is the observed intensity, y_b the estimated background, y_c the calculated intensity, and ϕ the peak profile function centered at 2θ.

These initial intensities can be generated automatically by the software (e.g., FullProf) from a known cell and space group, by placing idealized peaks and computing their areas.

The Le Bail method proves especially useful when working with powder X-ray data, where structural information is limited by factors such as: 1) low sensitivity to light elements, such as oxygen; 2) microabsorption and preferred-orientation effects, which affect the relative intensities of the peaks; 3) the presence of disordered phases or structural transitions that modify intensities without shifting peak positions. In these contexts, employing the Le Bail method allows accurate refinement of lattice parameters $(a, b, c, \alpha, \beta, \gamma)$, peak-profile characteristics (width, shape, asymmetry) and instrumental corrections such as zero-shift, all without introducing errors associated with poor determination of atomic positions. In contrast, for neutron data—where no appreciable preferred orientation exists and good sensitivity to light atoms is achieved—the full Rietveld refinement is more appropriate. In these cases, the intensities calculated from the structural model typically reproduce the observed ones well, enabling reliable refinement of atomic positions, occupancies and thermal parameters.

In conclusion, the combined use of the Rietveld method (for neutrons) and the Le Bail method (for X-rays) constitutes a complementary strategy that maximizes the information extracted from each technique: precise atomic-structure determination from neutrons, and fine structural evolution and reliable cell parameters from X-rays, even when intensities cannot be directly interpreted structurally.

Prior to commencing Rietveld refinements, we applied Le Bail refinement to the X-ray data to obtain more accurate cell parameters. We did not proceed with Rietveld refinement on those data because we could not achieve a good model to account for possible preferred orientations or other defects that prevented a satisfactory fit of the intensities.

3.5 *Amplimodes* in Structural Refinement

As introduced above, *amplimodes* represent collective normal displacement modes associated with the irreducible representations of the high-symmetry point group[29]. Although these modes are mathematically defined dynamically as time-harmonic oscillations via

$$u_i(t) = A_i \cos(\omega t + \phi), \tag{3.13}$$

where $u_i(t)$ is the displacement of atom i at time t, A_i the polarization vector, ω the angular frequency, and ϕ the phase, in the static structural analysis we are only concerned with the "frozen" configuration at $t = 0$.

At that instant, the static structural distortion can be expressed as a fixed displacement of the atoms from their high-symmetry positions, written as a linear combination of *amplimodes*:

$$\Delta \mathbf{r}_i = \sum_m A_m \, \mathbf{p}_i^{(m)}, \tag{3.14}$$

where $\Delta \mathbf{r}_i$ is the displacement of atom i, A_m the amplitude of mode m, and $\mathbf{p}_i^{(m)}$ the polarization vector of atom i in mode m. Consequently, the distorted structure $\mathbf{r}_i^{\text{dist}}$ is obtained by adding these displacements to the high-symmetry reference positions $\mathbf{r}_i^0$:

$$\mathbf{r}_i^{\text{dist}} = \mathbf{r}_i^0 + \sum_m A_m \, \mathbf{p}_i^{(m)}. \tag{3.15}$$

This formulation illustrates how the overall distortion decomposes into fundamental symmetry-imposed building blocks, simplifying both the physical interpretation and the refinement process. Instead of refining individual atomic coordinates, one refines the amplitudes A_m of the active *amplimodes*, yielding a more efficient and physically meaningful structural model.

3.5.1 Refinement with *amplimodes*

This formulation is key for the structural refinement based on *amplimodes*, since instead of refining directly the Cartesian or fractional coordinates of each atom, one refines only the amplitudes A_m of a reduced set of modes that account for the observed distortion[29]. This provides a much clearer and more compact physical description of the distorted structure.

Refining using *amplimodes* instead of atomic coordinates offers several important advantages:

1. **Parameter reduction:** rather than refining $3N$ atomic coordinates for N atoms, only the amplitudes of the active modes—usually far fewer—are refined. This improves numerical stability and avoids unnecessary overfitting.
2. **Direct physical interpretation:** each *amplimode* is tied to an irreducible representation of the space group, allowing one to clearly interpret which type of distortion (rotation, collective displacement, etc.) is occurring and how it affects structural and functional properties.
3. **Strict symmetry control:** *amplimodes* respect the constraints imposed by the lower-symmetry subgroup, preventing distortions incompatible with the symmetry and artificial symmetry breaking.
4. **Phase-transition analysis:** it enables monitoring the evolution of mode amplitudes with temperature, pressure, or other variables, facilitating the identification of critical modes and quantitative study of displacive transitions.
5. **Connection with group theory:** the description in terms of *amplimodes* directly links the refinement to theoretical concepts, easing systematic comparisons between materials and providing a reproducible and rigorous framework.

For the calculation of *amplimodes* from theoretical data, we used the `AMPLIMODES` tool of the Bilbao Crystallographic Server[29], starting from the high- and low-symmetry structures extracted from the ICSD database[52]. The resulting polarization vectors (V_x, V_y, V_z) were used directly as the starting point in FullProf for the *amplimode* refinement.

In the case of the Tb, Dy, and Ho molybdates, the structural distortion associated with the paraelectric–ferroelectric transition was described by the simultaneous activation of three sets of *amplimodes*:

- Γ_1**:** 14 initial amplitudes refined.
- Γ_3**:** 13 amplitudes, initially zero above 425K.
- $M_2^+ \oplus M_4$**:** 22 amplitudes, initially zero above 425K.

The amplitudes of Γ_3 and $M_2^+ \oplus M_4$ were set to zero at 425K; for successive temperatures, we copied the refined values from the previous step.

Further details on how we iteratively performed the *amplimode* refinement are provided below.

3.6 Refinement Assessment

Before considering the statistical parameters that quantify the quality of the fit in a Rietveld refinement, it is essential to perform a careful visual inspection of the diffraction pattern. Directly comparing the observed and calculated patterns allows one to immediately identify significant discrepancies, especially those associated with systematic errors that might escape numerical indicators.

This visual analysis is particularly useful for detecting peak profile mismatches, asymmetries, shifts, or poorly reproduced intensities, which may be related to issues in the structural modeling, instrumental defects, the presence of unmodeled phases, or an incorrect background model.

Therefore, visual evaluation constitutes a necessary preliminary step to validate the relevance of the refinement results and to guide any required improvements to the model.

Below are defined the four most commonly used parameters for quantitatively assessing the refinement:

Weighted profile R–factor:

$$R_{wp} = 100 \times \sqrt{\frac{\sum_i w_i \left(y_i^{\text{obs}} - y_i^{\text{calc}}\right)^2}{\sum_i w_i \left(y_i^{\text{obs}}\right)^2}}$$

Expected R–factor:

$$R_{\text{exp}} = 100 \times \sqrt{\frac{N - P}{\sum_i w_i \left(y_i^{\text{obs}}\right)^2}}$$

Reduced chi–square:

$$\chi^2 = \left(\frac{R_{wp}}{R_{\text{exp}}}\right)^2$$

Bragg R–factor:

$$R_{\text{Bragg}} = 100 \times \frac{\sum_k |I_k - I_k^{\text{calc}}|}{\sum_k |I_k|}$$

4 Analysis and Discussion of Results

Chapter 4 Summary

This section analyses the results of the refinement of X-ray diffraction patterns using the Le Bail method and neutron diffraction patterns using the Rietveld method for $Dy_2(MoO_4)_3$, $Ho_2(MoO_4)_3$ and $Tb_2(MoO_4)_3$. The good agreement between experimental and calculated data, together with low residuals and consistent reliability factors, indicates reliable refinements. The complementarity between both radiations for crystallographic analysis is confirmed, as their different interactions with matter lead to clear differences in the diffraction patterns. The evolution of the unit-cell parameters is studied as a function of temperature, hydrostatic pressure and chemical pressure. In the ferroelectric phase, where $b > a$, the contraction can be interpreted isotropically. Chemical pressure partly mimics the effect of hydrostatic pressure, although not always monotonically, while temperature produces a distinct behaviour, especially due to the anomalous expansion of the c parameter. The primary $M_2^+ \oplus M_4$ mode, which is central to the ferroelectric–ferroelastic transition, increases with decreasing volume, but decreases with rare-earth ionic radius, consistently with the reduction in transition temperature. The polar Γ_3 mode also tends to increase with decreasing temperature and ionic radius, although its behaviour is more complex. At the atomic level, the most relevant displacements correspond to oxygen atoms, providing a quantitative framework for understanding the structural mechanisms involved in the improper ferroelectric transition.

4.1 Discussion of the X-ray Diffraction Patterns

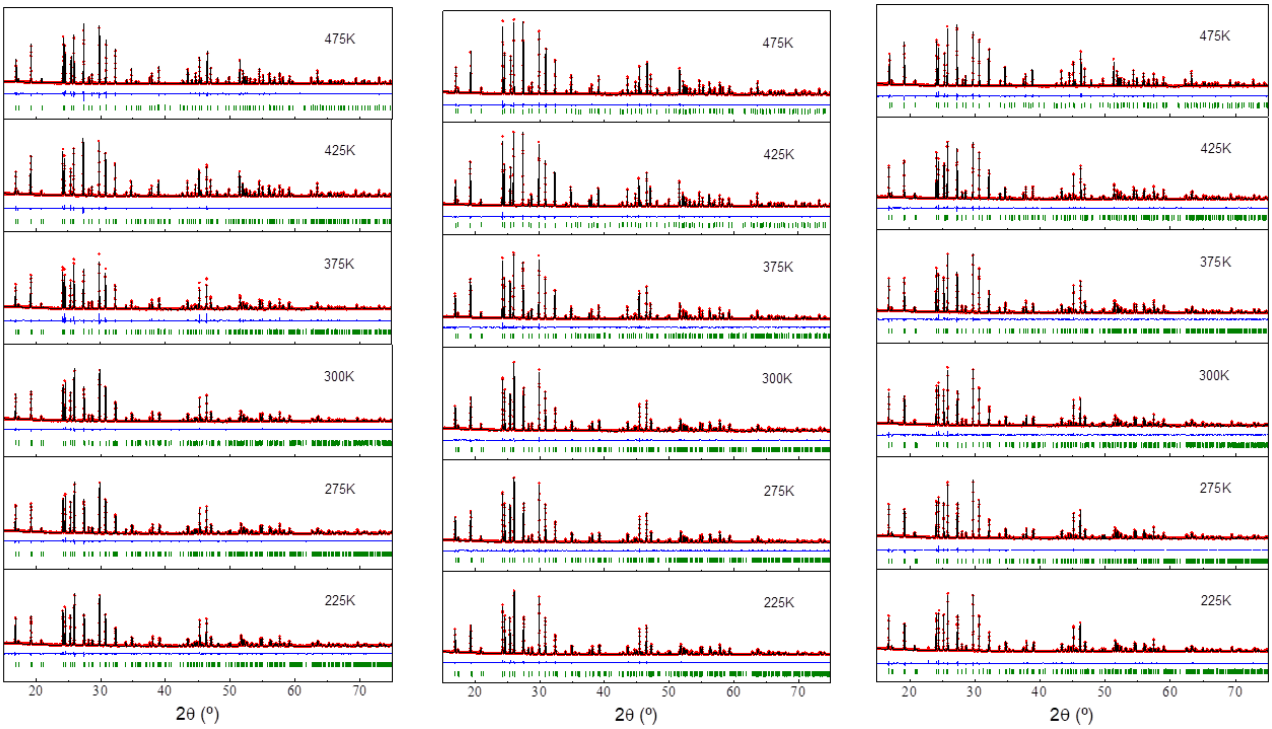

(a) $Dy_2(MoO_4)_3$ **(b)** $Ho_2(MoO_4)_3$ **(c)** $Tb_2(MoO_4)_3$

Figure 14: Le Bail full-profile refinement of the paraelectric and ferroelectric phases of $Dy_2(MoO_4)_3$ (a), $Ho_2(MoO_4)_3$ (b) and $Tb_2(MoO_4)_3$ (c) at 225, 275, 300, 375, 425 and 475 K. Observed experimental data (red), calculated profile (black), difference (calculated–observed) (blue), and Bragg positions (green) are shown.

The Le Bail refinement (full-profile) of the ferroelectric and paraelectric phases is shown in the plots of Figure 14(a,b,c). An excellent agreement is observed between the experimental values (red points) and the calculated ones (black line). The differences (blue line) remain small and without systematic features, indicating a reliable refinement. The peak positions match very well point-by-point between the observed and calculated patterns, and the intensities are also well reproduced for most peaks, especially at low and medium angles. The background appears well modeled, and the central region of the diffractograms refines better than the extremes. Peaks exhibit greater asymmetry at low angles and the background is more challenging to model, compounded by an excessive loss of intensity in those peaks affected by the atomic form factor at high angles.

The maximum and minimum reliability factors for all three compounds and temperatures are listed in Tables 1 and 2 (Appendix). The obtained values are similar to the Le Bail refinements performed by Gil de Cos on β'-$Y_2(MoO_4)_3$ [27].

There is barely any systematic shift of the peaks toward higher angles as temperature decreases, which would indicate a contraction of the cell parameters. The high-angle peaks show lower intensities mainly due to the angular dependence of the atomic form factor. The low scatter in the blue line (residuals) and the sharp definition of the peaks demonstrate that the photon count was high and the data quality excellent.

The separation of the peaks (without excessive overlap) allows subtle peaks corresponding to the ferroelectric phase to be observed, as indicated in Figure 15. When comparing across compounds, no clear shift associated with the contraction induced by chemical pressure is observed either.

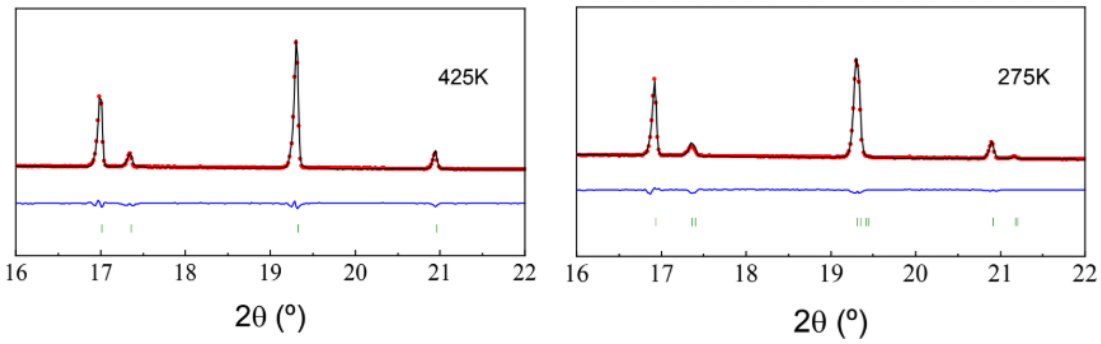

Figure 15: Rietveld refinement of $Ho_2(MoO_4)_2$ in the ferroelectric (left) and paraelectric (right) phases at 475 and 275 K. Observed data (red), calculated (black), difference (blue), and Bragg positions (green) are shown.

No atomic positions or thermal parameters were obtained, as only the profile was refined. In this respect, a clear trend of decreasing parameter U (associated with microstrain) is observed upon lowering the temperature in all three compounds. This suggests that, as the temperature increases, different regions of the crystal may expand non-uniformly, generating microstrains that could be related to the preparation for the phase transformation. In the paraelectric phase, this parameter generally tends to decrease again.

4.2 Discussion of Neutron Diffraction Patterns

The Rietveld refinement of the ferroelectric and paraelectric phases is shown in Figure 16. Excellent agreement is observed between the experimental data (red points) and the calculated pattern (black line). The difference curve (blue line) remains small and free of systematic deviations, indicating a reliable refinement. Peak positions match very accurately between observed and calculated patterns, and the intensities are well reproduced for most peaks, especially at low and medium angles. The background appears well modeled, and the central region of the diffraction patterns refines better than the edges (see Section 2.2.3).

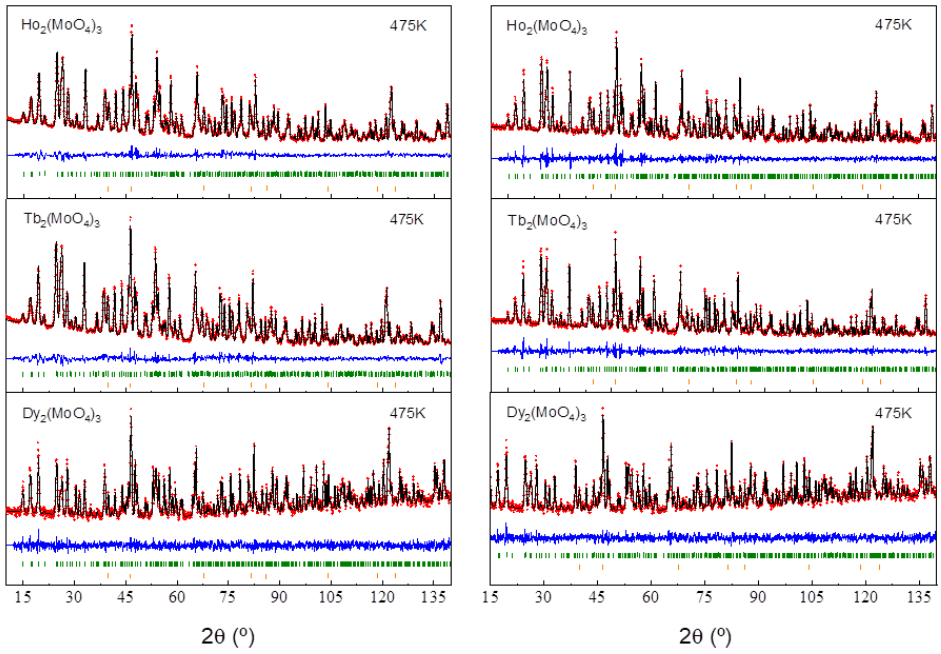

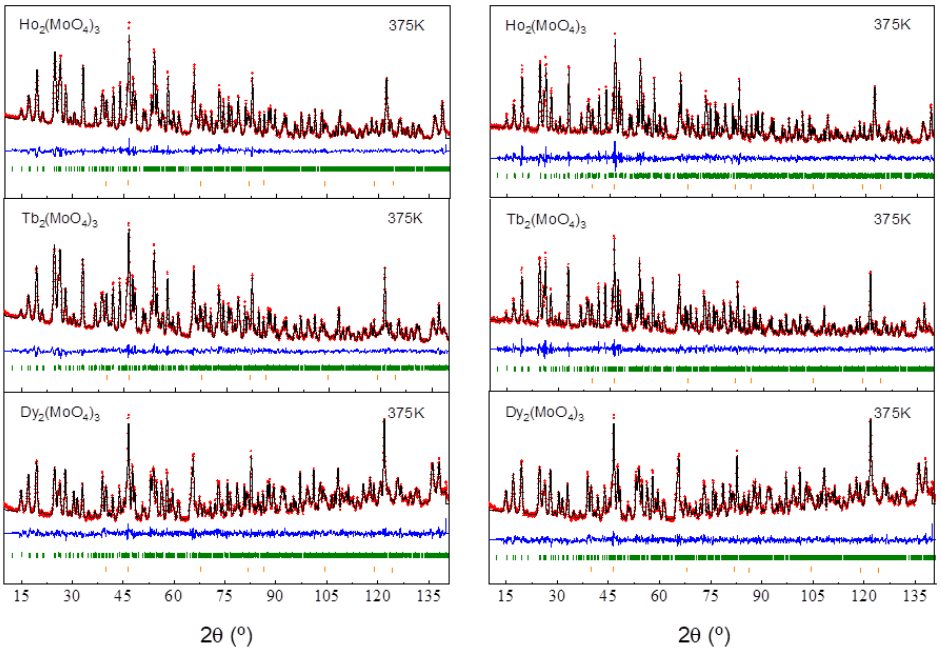

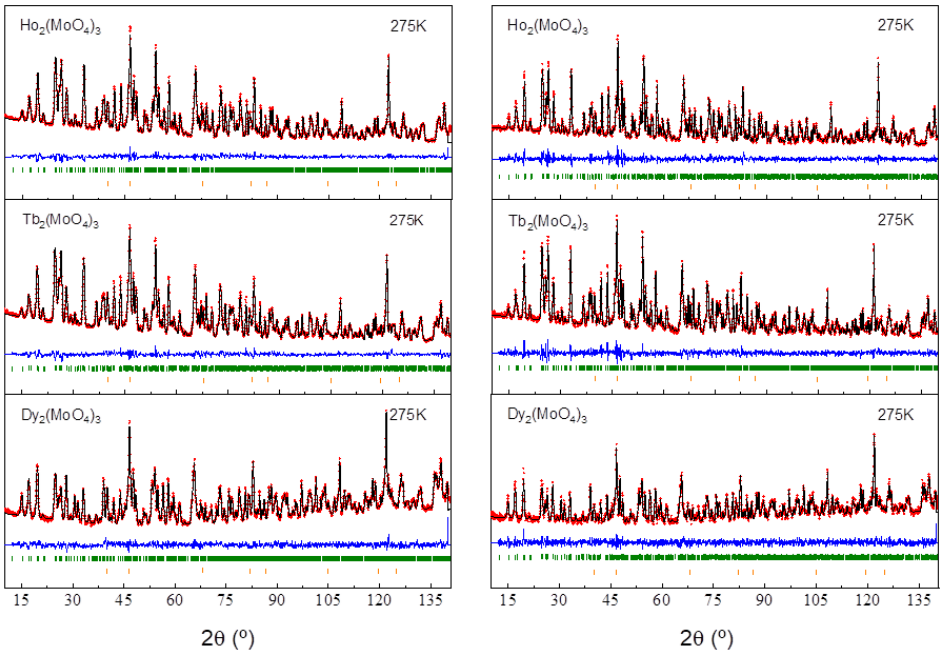

Figure 16: Rietveld refinement with neutrons at 475K (top), 375K (middle) and 275K (bottom) of the diffraction patterns of $Dy_2(MoO_4)_3$, $Ho_2(MoO_4)_3$ and $Tb_2(MoO_4)_3$. Shown are the experimental data (red), calculated (black), the difference (blue), and the Bragg positions (green and orange).

The maximum and minimum values of the reliability factors for all three compounds and across all temperatures are listed in Tables 1 and 2 (Appendix). These values can be compared with similar refinements in the literature[57].

First, note the difference between the plots on the left (full detector) and on the right (detector center). The peak intensities nearly triple when integrating over the entire detector, improving counting statistics compared to the patterns on the right, which only use the detector center. Although these central-detector patterns yield lower counts and a reduced signal-to-noise ratio, their peaks are sharper and thus provide higher angular resolution.

A second set of reflections (in red) is also visible alongside those corresponding to the studied molybdate phases (in green). These extra peaks arise from the aluminum sample holder used in the D2B diffractometer. Since this phase is minor and yields low count statistics, its individual refinement is less precise than that of the main phases. We improved the robustness of its refinement by performing a simultaneous multi-pattern fit of all six neutron diffraction datasets collected at the same temperature, fixing the aluminum cell parameters and atomic coordinates to the same values across all patterns. This strategy stabilized the refinement of the minor phase despite its limited peak intensity.

As with the X-ray patterns, there is almost no systematic peak shift to higher angles as temperature decreases—a signature of cell-parameter contraction. However, in this case the high-angle peaks do not lose intensity (see Sec. 2.2.2), although they do lose resolution, as shown in Fig. 17 when detecting the ferroelectric peaks. Comparing across compounds, no clear shift due to chemical-pressure-induced contraction is observed either.

Distinguishing among the three rare-earth molybdates, we see that the peak intensities in the Dy compound decrease markedly. This is due to differences in both coherent and incoherent neutron scattering lengths: Dy has a coherent length of 16.9 fm but an incoherent scattering length of 12.8 fm, whereas Tb (7.38 fm coherent, <1 fm incoherent) and Ho (8.01 fm coherent, <1 fm incoherent) show much lower incoherent contributions. The higher incoherent scattering in Dy increases background noise and reduces peak definition. Additionally, Dy's thermal-neutron absorption cross-section (994 barn) is far greater than that of Tb (23 barn) and Ho (64.7 barn). To prevent intensity loss from adversely affecting the thermal-vibration ellipsoids—which in Dy showed unphysical negative components—we initially refined a global scale-factor exponential term during the early refinement stages and then fixed it thereafter. The poorer quality of the Dy molybdate data led to larger standard uncertainties and less systematic temperature-dependent behavior of the structural parameters.

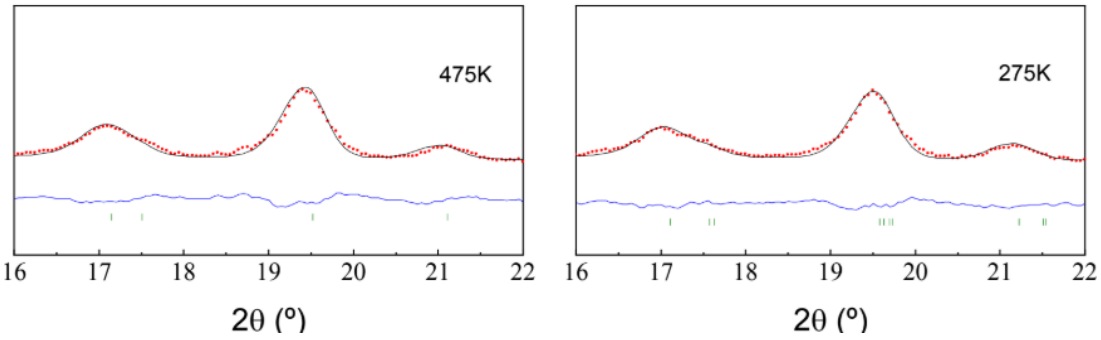

Figure 17: Refinement of $Tb_2(MoO_4)_2$ in the ferroelectric (left) and paraelectric (right) phases at 475 and 275 K. Shown are observed data (red), calculated (black), their difference (blue), and Bragg positions (green).

While the U parameter obtained from X-ray diffraction shows a decreasing trend with temperature—behavior expected due to the relaxation of thermal microstrains—in the neutron data this parameter increases as temperature decreases. This discrepancy suggests that X-ray diffraction provides a more consistent description of the microstructural evolution in these compounds, possibly due to its higher sensitivity to thermally induced local distortions and a better signal-to-noise ratio in the analyzed reflections.

4.3 Discussion of Lattice Parameters, $b - a$ Differences, and Global *Amplimodes*

In the following we discuss how the crystal structures of the improper ferroelectric molybdates $RE_2(MoO_4)_3$ respond to three physical conditions—temperature, hydrostatic pressure, and chemical pressure—using comparable variables: the unit-cell volume, the lattice parameters a, b, and c, the difference $b - a$, and the structural *amplimodes* $M_2^+ \oplus M_4$ (primary) and Γ_3 (secondary).

In Figure 18 we plot the evolution of the lattice parameters a, b, and c as functions of unit-cell volume based on experimental data collected between 225 K and 475 K for the three molybdates $Tb_2(MoO_4)_3$ (red), $Dy_2(MoO_4)_3$ (green), and $Ho_2(MoO_4)_3$ (blue). We also compare these with the theoretical hydrostatic-pressure simulations of the paraelectric phase (pink) and the ferroelectric phase (violet) reported by our group in a previous study[58]. Black and orange guide-lines are included to highlight the parameter changes between 225 K and 475 K.

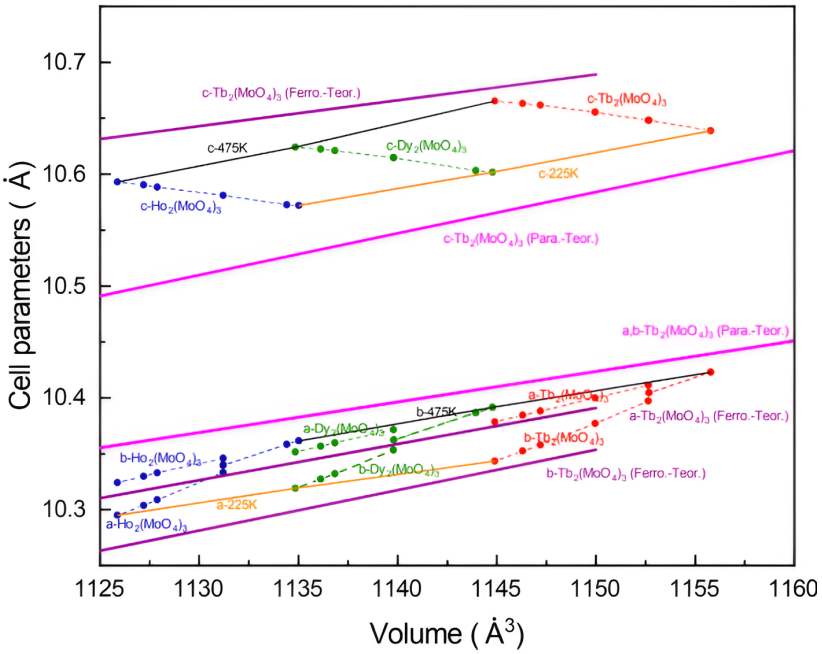

Figure 18: Evolution of the lattice parameters a, b, and c versus unit-cell volume for experimental data collected between 225K and 475K for $Tb_2(MoO_4)_3$ (red points), $Dy_2(MoO_4)_3$ (green points), and $Ho_2(MoO_4)_3$ (blue points), and for the theoretical simulations of the β-$Tb_2(MoO_4)_3$ phase (solid pink line) and the β'-$Tb_2(MoO_4)_3$ phase (solid violet line). Black and orange guide-lines connect the 475K and 225K data to illustrate the evolution of the lattice parameters under chemical pressure.

The lattice parameters a and b contract with decreasing volume in all systems (experimental and theoretical). In the ferroelectric phase, a clear separation between a and b ($b > a$) is observed, becoming more pronounced as the volume decreases (lower T). In the paraelectric phase, $a = b$, reflecting tetragonal symmetry. The parameter c (the polar axis) increases in the experimental data as temperature decreases (volume decreases), which is opposite to the behavior under hydrostatic pressure (according to the theoretical data), where c decreases.

One can also approximately identify the paraelectric–to–ferroelectric phase transition temperatures from the experimental measurements. This behavior is typical of these compounds[23], but the evolution under hydrostatic, chemical, and thermal pressure had not been directly compared. The response to reducing both types of pressure is very similar, so decreasing the rare-earth ionic radius produces an effect on the crystal structure broadly analogous to hydrostatic pressure. The contraction of the experimental cell parameters a, b, and c for all the molybdates occurs from the values of the theoretical paraelectric phase (larger) toward those of the theoretical ferroelectric phase (smaller).

This behavior can be explained by noting that, for a given molar volume or number of atoms, higher-symmetry structures—such as the paraelectric phase—tend to require larger unit cells to maintain that symmetry, especially when the lattice must accommodate atoms in highly ordered positions, which typically implies larger interatomic separations. In contrast, lower-symmetry structures, such as the ferroelectric ones, present more structural degrees of freedom—both in lengths and angles of the cell—allowing greater relaxation and compaction of the system as it optimizes its internal energy. This coherence between the experimentally observed structural changes and those predicted by the theoretical models demonstrates that the calculations faithfully reproduce the real structural trends, thereby confirming their great utility and reliability for the study of phase transitions and complex crystallographic properties.

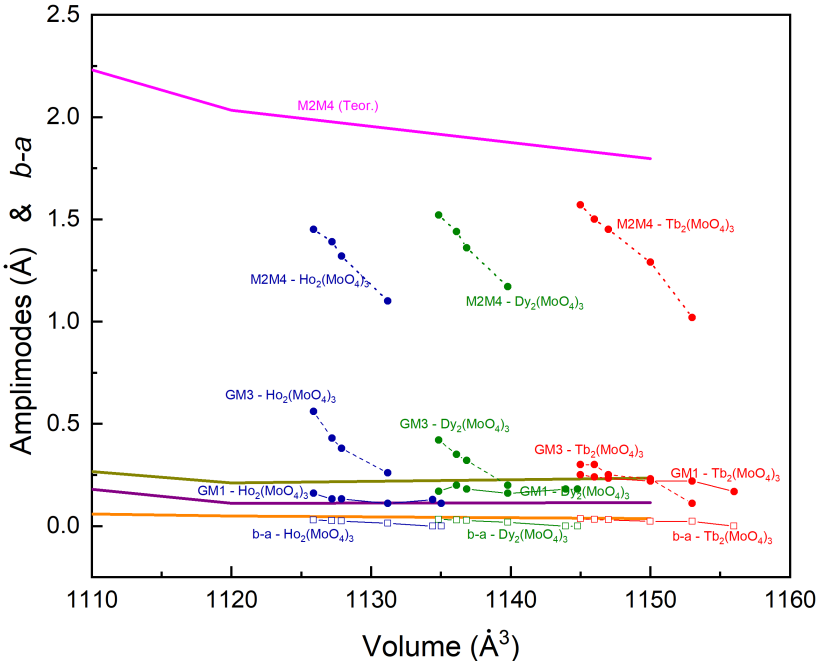

Figure 19: Global amplitudes of the Γ_1, $M_2^+ \oplus M_4$ and Γ_3 modes and the difference $b - a$ versus unit cell volume for the theoretical ferroelectric phases of $Tb_2(MoO_4)_3$ (from top to bottom: pink, dark green, dark violet and orange for the $M_2^+ \oplus M_4$, Γ_1, Γ_3 modes and $b - a$, respectively) and for the experimental ferroelectric phases of $Tb_2(MoO_4)_3$ (red), $Dy_2(MoO_4)_3$ (green) and $Ho_2(MoO_4)_3$ (blue). The colors were chosen to match those used in the cell parameter plots.

In Figure 19 we present the global amplitudes of the displacements with symmetries Γ_1, $M_2^+ \oplus M_4$ and Γ_3 starting from the paraelectric phase of $Tb_2(MoO_4)_3$, both for the theoretically simulated ferroelectric phases (pink and violet tones) and for the experimental ferroelectric phases of the Tb (green tones), Dy (blue tones) and Ho (red tones) molybdates. We also plot the quantity $b-a$, which is highly sensitive to symmetry breaking. As expected (see Section 1.5.3), the primary non-polar mode $M_2^+ \oplus M_4$ has a larger amplitude than the secondary modes Γ_1 and Γ_3, which themselves differ but to a lesser extent. The amplitude of the primary mode that triggers the improper ferroelectric transition, $M_2^+ \oplus M_4$, increases as the experimental volume (temperature) and theoretical volume (hydrostatic pressure) decrease.

However, it decreases when the ionic radius is reduced (Ho shows a smaller $M_2^+ \oplus M_4$ amplitude than Dy and Tb), indicating that chemical pressure does not favor this distortion.

These findings are consistent with the evolution of $b - a$: $b - a > 0$ in all cases, following a trend very similar to that of the $M_2^+ \oplus M_4$ mode, which suggests that $b - a$ can serve as an indirect indicator of the primary mode's amplitude. Under decreasing temperature and hydrostatic pressure, $b-a$ increases significantly, but upon reducing the ionic radius (Ho>Dy>Tb) it decreases, although this latter trend is not perfectly monotonic, mirroring the behavior of the global $M_2^+ \oplus M_4$ mode.

This result agrees with the fact that ferroelectric molybdates containing smaller-radius rare earths exhibit lower phase transition temperatures[59], consistent with the characteristics of "displacive" transitions[10].

The Γ_3 mode, a secondary polar mode responsible for the emergence of spontaneous polarization (see Section 1.5.3), shows a monotonically increasing amplitude as temperature decreases; however, it also increases when the ionic radius is reduced. Furthermore, for the Dy and Ho molybdates it exceeds the amplitude of the Γ_1 mode, whereas for Tb (both experimental and theoretical) it is comparable or lower, respectively. It would be interesting to perform theoretical calculations for Ho and Dy to confirm this trend.

This behavior is echoed in the $La_xEr_{2-x}(MoO_4)_3$ solid solutions, where increasing Er content enhances the Γ_3 mode and the remanent and saturation polarization values obtained from ferroelectric hysteresis loops[28]. The Γ_1 mode is less significant since it depends on the paraelectric reference structure and does not participate in the phase transition (these displacements do not break paraelectric symmetry).

Moreover, the theoretical values of Γ_1 and Γ_3 exhibit a concave trend: Γ_3 initially decreases with volume and then increases again, possibly indicating an intermediate energy minimum or high sensitivity to slight structural variations. This complexity suggests that Γ_3 is not activated directly by volume change, but rather through coupling with the primary mode and the surrounding structural environment. In principle, the Dy and Ho molybdates could also display concave Γ_3 behavior under hydrostatic pressure, given their similar structural sensitivity and mode–mode coupling exhibited by the Tb molybdate. This would be worth verifying through dedicated theoretical studies.

4.4 Individual *amplimodes* and structural mechanisms

In Figures 20, 21 and 22, the displacement vectors corresponding to the symmetry mode $M_2^+ \oplus M_4$ are shown, calculated for the compounds $Ho_2(MoO_4)_3$, $Dy_2(MoO_4)_3$ and $Tb_2(MoO_4)_3$.

These vectors indicate the atomic displacements from the paraelectric to the ferroelectric phase within the unit cell. On the left of each figure the structure at 225K is displayed, and on the right at 375K. The top views are perpendicular to the a-axis, while the bottom views are perpendicular to the c-axis.

In the central plot, the individual amplitudes of the modes with the same symmetry ($M_2^+ \oplus M_4$) are plotted as a function of unit-cell volume. Dashed vertical lines mark the volumes corresponding to 225K and 375K, and a color code identifies the different atom types in the crystal. Overall, a very similar behavior is observed in all three compounds, consistent even with the theoretical predictions.

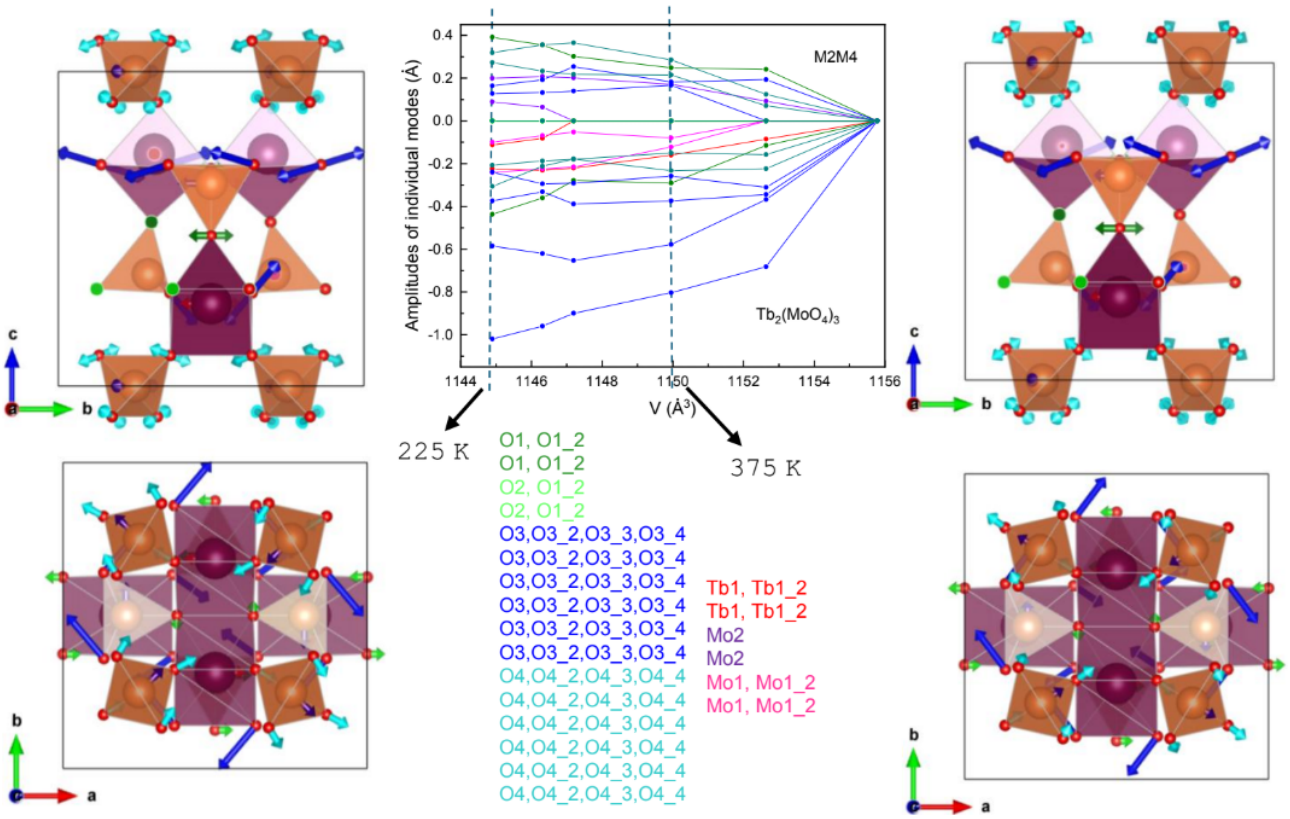

Figure 20: Displacement vectors compatible with the $M_2^+ \oplus M_4$ symmetry mode of $Tb_2(MoO_4)_3$: left at 225K and right at 375K. In the center, the mode amplitudes are plotted against unit-cell volume for all atoms, using the color code indicated.

Oxygen atoms display larger displacements (amplitudes) compared to heavier elements such as Ho, Dy, Tb and Mo, which is to be expected given their lower mass.

This result partially contrasts with the recent work of Nylund *et al.*[24], who calculate the ferroelastic strain from the thermal evolution of the lattice parameters and, via Rietveld refinements of temperature-dependent X-ray diffraction data, observe that the different cations exhibit distinct critical behaviors. However, we have found that neutron diffraction data allow a more precise determination of atomic positions, and that using *amplimodes* provides a clearer hierarchy of atomic displacements, improving the structural refinement compared to the conventional coordinate-based approach.

Among the oxygens, those of type O2 (light green)—which form part of the shared edge of the rare-earth dimer—exhibit the smallest displacements, likely due to structural constraints in that region. The displacement amplitudes of oxygens O1 (dark green) and O4 (light blue) are similar; both connect Mo and rare-earth atoms along the c axis. The O1 oxygens displace mainly along a and b, whereas the O4 oxygens show a small c-component and a more pronounced displacement along the ab diagonal.

The most significant displacements correspond to the O3 oxygens (navy blue), which also lie along the ab diagonal, with an additional c-component that decreases as the temperature increases. This component is particularly notable in the theoretically simulated compound under negative pressure, showing a trend similar to the experimental behavior when pressure is reduced. In particular, the displacement component along b is larger than that along a, revealing an anisotropy in the structural distortion. This is consistent with the fact that $b > a$.

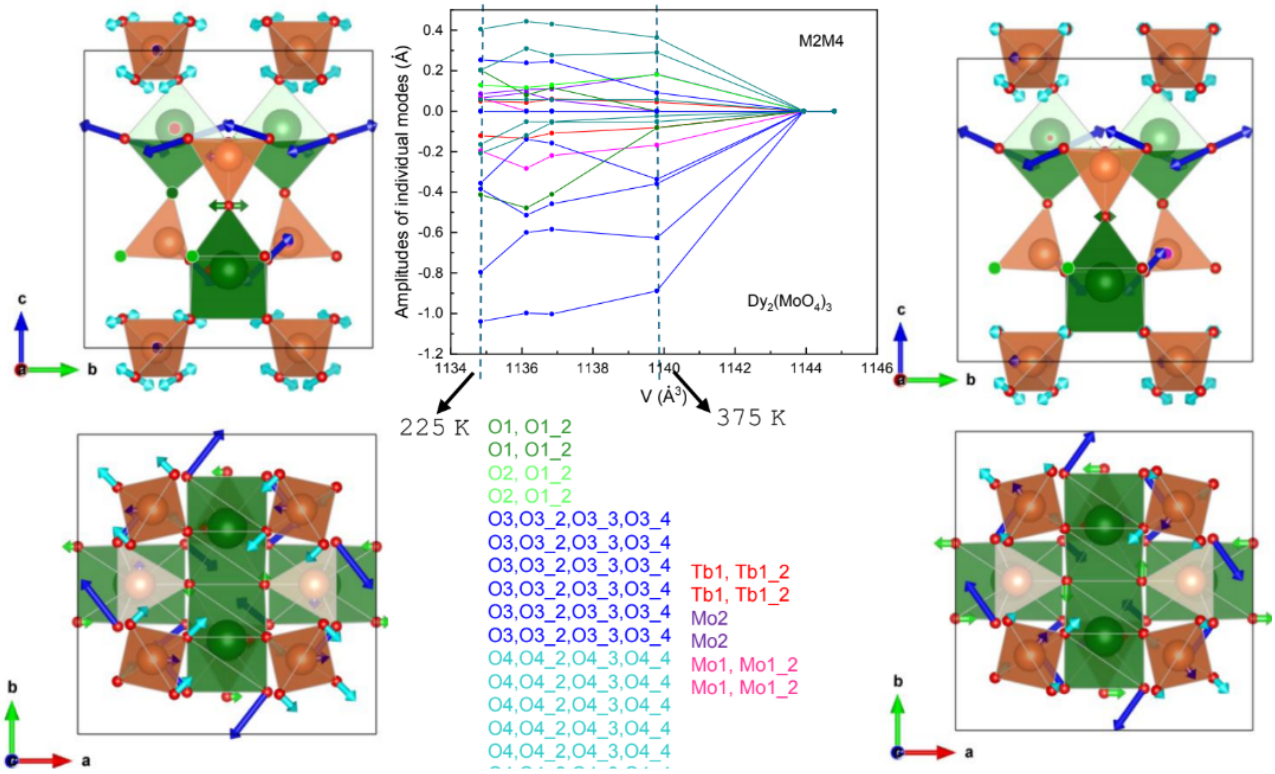

Figure 21: Displacement vectors compatible with the $M_2^+ \oplus M_4$ symmetry mode of $Dy_2(MoO_4)_3$: on the left at 225K and on the right at 375K. In the center, the mode amplitudes are plotted against unit-cell volume, with different atom types indicated by the color code shown.

Furthermore, it is observed that when the rare-earth cation is replaced by one with a larger ionic radius, the individual displacements associated with the $M_2^+ \oplus M_4$ mode also increase, similarly to the behavior described for the global modes. The decrease in ionic radius favors a structure with smaller differences between the sizes of the MoO_4 tetrahedra and the REO_7 polyhedra, which could restrict oxygen movements in less distorted structures (with smaller differences between a and b). This reduction in mode amplitudes suggests a chemical pressure effect that stabilizes the higher-symmetry (paraelectric) phase at lower temperatures.

We have also examined the temperature dependence of the amplitudes and directions of the displacements compatible with the polar symmetry mode Γ_3. In this case, no conclusions as clear as for the $M_2^+ \oplus M_4$ mode could be drawn, likely because these displacements are roughly an order of magnitude smaller, with comparable standard deviations. Moreover, their magnitude is similar to that of the thermal displacements refined under the paraelectric phase symmetry. Several refinements were performed, but they did not always yield consistent results. No clear pattern emerges in the behavior across the three compounds, nor is there an obvious correspondence with the theoretical predictions. Further investigation will be necessary to understand the increase in the global Γ_3 mode amplitude as the rare-earth ionic radius decreases and to explain the anomalies observed in the theoretical calculations. It would also be valuable to compare with theoretical calculations for other rare-earth elements.

Similarly, it would be helpful to revisit the experimental refinements in which modes with very small amplitudes and/or large uncertainties were omitted. Finally, plotting bond lengths to correlate more precisely the observed displacements with bond contractions or elongations—and with changes in bond angles—would be advisable. This analysis should focus especially on the polyhedral environments and the oxygen bridges connecting those polyhedra.

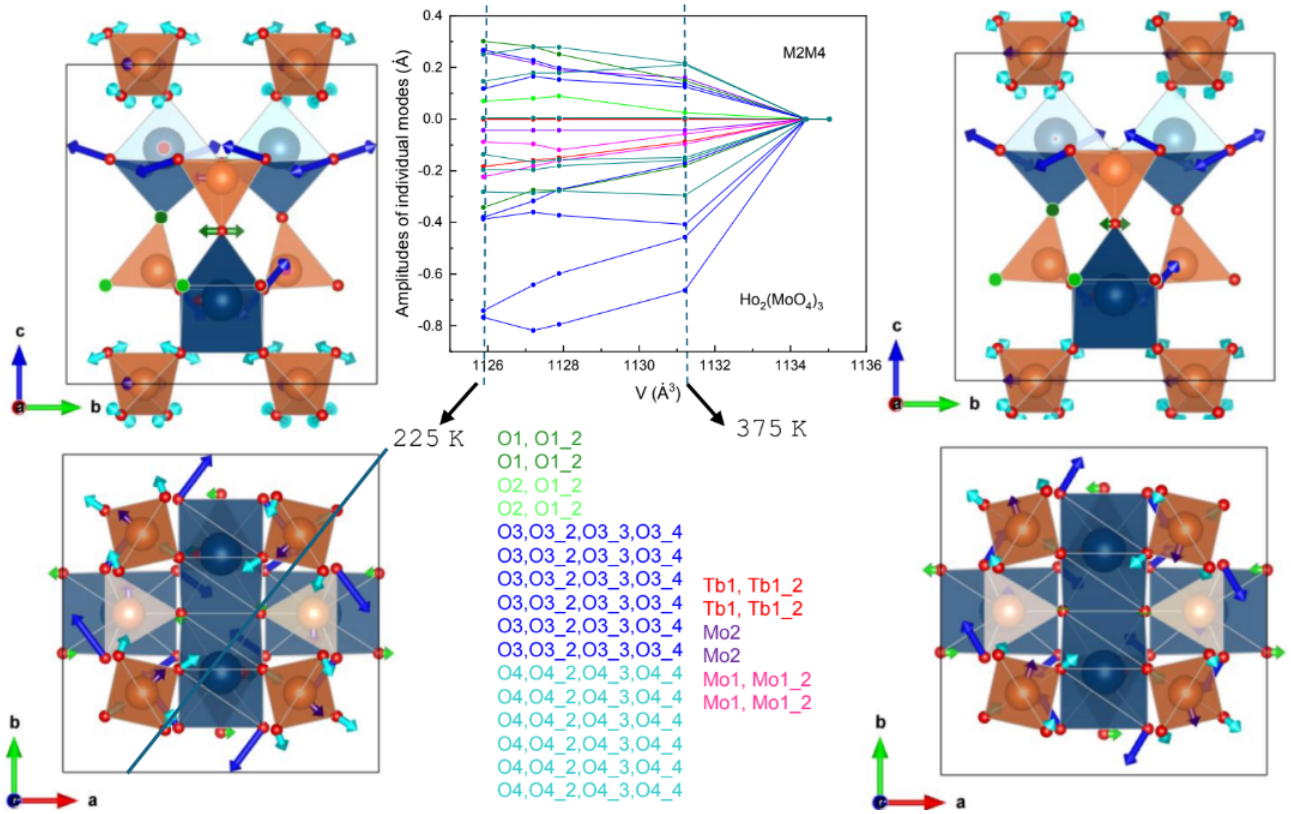

Figure 22: Displacement vectors compatible with the $M_2^+ \oplus M_4$ symmetry mode of $Ho_2(MoO_4)_3$, shown at 225K (left) and 375K (right). In the center, the mode amplitudes are plotted against unit-cell volume for all modes, with different atom types distinguished by the indicated color code.

5 Conclusions and Future Work

Chapter 5 Summary

The study highlights the importance of rigorous planning and careful selection of improper ferroelectric $RE_2(MoO_4)_3$ compounds ($RE = Tb, Dy, Ho$) for reliable comparative analysis. The combination of X-ray and neutron diffraction enabled accurate structural refinement and the identification of distortion modes related to the ferroelectric transition. It was observed that structural distortion increases with volume reduction, whether induced by temperature or pressure, while chemical pressure tends to stabilise the paraelectric phase. The polar mode responsible for spontaneous polarization shows complex behaviour linked to its interaction with other structural modes. Overall, the experimental and theoretical results show good consistency, validating the comparative approach and contributing to a deeper understanding of improper ferroelectricity in these materials.

5.1 Conclusions

This study highlights the importance of rigorous planning from the initial stages of research to ensure scientific consistency. The selection of the $RE_2(MoO_4)_3$ series (RE = Tb, Dy, Ho)—improper ferroelectrics with consecutive ionic radii—provided a solid basis for a detailed comparative analysis. The reproducible synthesis of these phases, combined with an experimental design that leverages the complementarity of X-ray diffraction (sensitive to heavy elements) and neutron diffraction (sensitive to light elements), enabled the collection of reliable data and accurate structural interpretation. The careful choice of rare earths with low neutron absorption—excluding elements such as Gd, Eu, or Sm—reflects a consciously optimized experimental plan.

Rietveld multipattern refinements, simultaneously combining X-ray and neutron diffraction patterns for the three phases at the same temperature, proved to be a key tool for structural analysis. This approach enabled the coherent and accurate refinement of shared parameters, although it required special attention to background and profile modeling due to the inherent differences between both techniques. The incorporation of the Le Bail method was necessary to correct preferred orientation in the absence of a suitable structural model, while the use of amplimodes allowed for a faithful representation of the distortions associated with ferroelectric transitions, surpassing conventional refinements based on atomic coordinates. This facilitated the identification and tracking of the key active modes as a function of temperature, reinforcing the methodological approach adopted.

The structural refinements showed excellent agreement with the experimental data, yielding low residuals and no systematic deviations, comparable to reference studies on complex ferroelectrics. Neutron diffraction played a crucial role in detecting light atoms such as oxygen, although the signal for Dy was limited by its high absorption and incoherent scattering—an aspect carefully considered in the interpretation. Furthermore, the evolution of microstructure with temperature was consistently interpreted, as evidenced by changes in peak widths, particularly in the X-ray data.

Comparison between experimental results and theoretical models for $Tb_2(MoO_4)_3$ revealed significant structural coherence under different types of compression (thermal, chemical, and hydrostatic). The cell parameters a and b contract upon volume reduction, maintaining the orthorhombic distortion ($b > a$) in the ferroelectric phase, which disappears upon transition to the tetragonal paraelectric phase ($a = b$). The c parameter exhibited opposite behavior experimentally (expanding upon cooling) and theoretically under pressure (contracting), revealing subtle differences between compression modes. Chemical substitution with smaller-radius rare earths reproduced structural effects analogous to external pressure, validating the comparative approach.

The trajectory from more symmetric, expanded structures to more compact, distorted configurations upon volume reduction reflects a relaxation consistent with symmetry breaking and reaffirms the predictive power of the calculations.

Regarding symmetry modes, the nonpolar primary mode $M_2^+ \oplus M_4$ and the polar secondary mode Γ_3 evolve in a correlated manner, decisively influencing the crystal symmetry and ferroelectric properties. The parameter $b - a$, sensitive to symmetry breaking, accurately tracks the evolution of the primary mode responsible for the improper ferroelectric transition, whose amplitude increases with decreasing experimental (thermal) and theoretical (hydrostatic) volume, indicating greater structural distortion. In contrast, chemical pressure stabilizes the paraelectric phase, reducing that distortion as the ionic radius decreases (Ho $<$ Dy $<$ Tb).

The polar mode Γ_3, responsible for spontaneous polarization, shows a more complex evolution: its amplitude increases upon cooling and, unexpectedly, also grows with decreasing ionic radius, as seen in similar solid solutions and macroscopic properties. However, its magnitude is roughly an order of magnitude smaller and comparable to thermal displacements, making firm conclusions difficult with the current refinements. Theoretical calculations indicate that the Γ_1 and Γ_3 modes exhibit a nonlinear volume dependence, suggesting energetic minima and sensitivity to small structural variations. This implies that Γ_3 is not activated directly by volume changes but via coupling with the primary mode and the structural environment, opening the door to complex phenomena in the ferroelectric transition.

5.2 Future Work

To further understand the structural mechanisms involved in the ferroelectric transition of $RE_2(MoO_4)_3$, we propose a detailed analysis of bond lengths and angles, precisely correlating atomic displacements with bond contractions or expansions. This study should focus especially on the polyhedral environments and the oxygen bridges connecting these polyhedra, which are key to understanding structural distortions.

DFT simulations under negative pressure confirmed the general experimental trends, although the polar mode Γ_3 exhibited a non-monotonic volume dependence, indicating the need for additional studies. In this regard, we recommend extending theoretical calculations to the Dy and Ho compounds and analyzing less obvious secondary structural modes to optimize our understanding of these materials.

For data analysis, it would be useful to compute distortion indices specific to the MoO_4 and REO_n groups and correlate them with the amplitudes of the $M_2^+ \oplus M_4$ and Γ_3 modes. We also suggest plotting uncertainty bands for the Γ_3 mode, obtained from grouped refinements, and comparing them with theoretical predictions. Applying multivariate techniques, such as principal component analysis (PCA) or clustering, on key variables—vibrational modes, distortions, $b - a$, ionic radius, and volume—would help identify hidden patterns and relevant correlations. Additionally, overlaying data from analogous series as a function of ionic radius, with an emphasis on visualizing oxygen displacement vectors, would aid in detecting significant local structural differences.

Finally, we propose measuring ferroelectric hysteresis loops at different temperatures for the entire $RE_2(MoO_4)_3$ family. Unlike earlier studies that required single crystals, which are difficult to obtain, these measurements can now be feasibly carried out on crystalline powders. This would allow us to assess whether, as observed in the solid solution $La_xEr_{2-x}(MoO_4)_3$, the polar mode exhibits atypical behavior, with spontaneous polarization increasing as the ionic radius decreases—even by an order of magnitude. Confirming this effect would be highly significant, as it would enable the tuning of improper ferroelectricity through ionic radius adjustment. With this understanding, other material families with technological potential based on this property could be explored and optimized.

6 References

[1] B. Dunn, H. Kamath, and J. M. Tarascon, "Electrical energy storage for the grid: a battery of choices," *Science*, vol. 334, pp. 928–935, 2011. https://doi.org/10.1126/science.1212741

[2] S. P. Beeby, M. J. Tudor, and N. M. White, "Energy harvesting vibration sources for microsystems applications," *Meas. Sci. Technol.*, vol. 17, no. 12, pp. R175–R195, 2006. https://doi.org/10.1088/0957-0233/17/12/R01

[3] L. L. Nagornaya, F. A. Danevich, A. M. Dubovik, B. V. Grinyov, S. Henry, V. Kapustyanyk, *et al.*, "Tungstate and molybdate scintillators to search for dark matter and double beta decay," *IEEE Trans. Nucl. Sci.*, vol. 56, no. 4, pp. 2513–2518, 2009. https://ieeexplore.ieee.org/document/5204623

[4] E. V. Zharikov, C. Zaldo, and F. Diaz, "Double tungstate and molybdate crystals for laser and nonlinear optical applications," *MRS Bull.*, vol. 34, no. 4, pp. 271–276, 2009.

[5] Z. Wang, H. Wu, G. W. Burr, C. S. Hwang, K. L. Wang, Q. Xia, and J. J. Yang, "Resistive switching materials for information processing," *Nature Reviews Materials*, vol. 5, no. 3, pp. 173–195, 2020. https://doi.org/10.1038/s41578-019-0159-3

[6] V. Wadhawan, *Introduction to Ferroic Materials*, CRC Press, 2000. https://doi.org/10.1201/9781482283051

[7] "Showing relationship between ferroelectric, ferro-elastic and ferromagnetic materials (Figure 1)," *ResearchGate*, accessed July 6, 2025. https://www.researchgate.net/figure/showing-relationship-between-ferroelectric-ferro-elastic-ferromagnetic-materials$_fig1_3$69505869

[8] G. Shirane, F. Jona, and R. Pepinsky, "Some aspects of ferroelectricity," *Proceedings of the IRE*, vol. 43, no. 12, pp. 1738–1793, 1955. https://doi.org/10.1109/JRPROC.1955.278041

[9] K. Aizu, "Possible species of 'ferroelastic' crystals and of simultaneously ferroelectric and ferroelastic crystals," *Journal of the Physical Society of Japan*, vol. 27, no. 2, pp. 387–396, 1969. https://doi.org/10.1143/JPSJ.27.2.387

[10] S. C. Abrahams, "Structure relationship to dielectric, elastic and chiral properties," *Acta Crystallogr. A*, vol. 50, pp. 658–666, 1994. https://doi.org/10.1107/S0108767394011286

[11] F. R. M. Hitchcock, "The tungstates and molybdates of the rare earths," *J. Am. Chem. Soc.*, vol. 17, p. 520, 1895. https://doi.org/10.1021/ja02162a006

[12] H. J. Borchardt and P. E. Bierstedt, "$Gd_2(MoO_4)_3$: a ferroelectric laser host," *Appl. Phys. Lett.*, vol. 8, p. 50, 1966. https://doi.org/10.1063/1.1754477

[13] W. Jeitschko, "Crystal structure of $La_2(MoO_4)_3$, a new ordered defect scheelite type," *Acta Crystallogr. B*, vol. 29, pp. 2074–2081, 1973. http://scripts.iucr.org/cgi-bin/paper?S0567740873006138

[14] J. D. Axe, B. Dorner, and G. Shirane, "Mechanism of the ferroelectric phase transformation in rare-earth molybdates," *Phys. Rev. Lett.*, vol. 26, no. 9, p. 519, 1971. https://doi.org/10.1103/PhysRevLett.26.519

[15] J. S. O. Evans, T. A. Mary, and A. W. Sleight, "Negative thermal expansion in $Sc_2(WO_4)_3$," *J. Solid State Chem.*, vol. 137, no. 1, pp. 148–160, 1998. https://www.sciencedirect.com/science/article/pii/S0022459698977441

[16] B. A. Marinkovic, M. Ari, R. R. de Avillez, F. Rizzo, F. F. Ferreira, K. J. Miller, *et al.*, "Correlation between AO_6 polyhedral distortion and negative thermal expansion in orthorhombic $Y_2Mo_3O_{12}$ and related materials," *Chem. Mater.*, vol. 21, no. 13, pp. 2886–2894, 2009. https://doi.org/10.1021/cm900650c

[17] C. Guzmán-Afonso, C. González-Silgo, J. González-Platas, M. E. Torres, A. D. Lozano-Gorrín, N. Prado Sabalisck, V. Sánchez-Fajardo, J. Campo, and J. Rodríguez-Carvajal, "Structural investigation of the negative thermal expansion in yttrium and rare earth molybdates," *J. Phys.: Condens. Matter*, vol. 23, p. 325402, 2011. https://doi.org/10.1088/0953-8984/23/32/325402

[18] C. Guzmán-Afonso, M. E. Torres, C. González-Silgo, N. Prado Sabalisck, J. González-Platas, E. Matesanz, and A. Mujica, "Electrical transport and anomalous structural behavior of -$Eu_2(MoO_4)_3$ at high temperature," *Solid State Commun.*, vol. 151, pp. 1654–1658, 2011. https://doi.org/10.1016/j.ssc.2011.08.009

[19] N. Prado Sabalisck, G. Gil-de-Cos, C. González-Silgo, C. Guzmán-Afonso, V. Lavín, J. López-Solano, I. T. Martín-Mateos, L. Mestres, A. Mujica, D. Santamaría-Pérez, M. E. Torres, and X. Vendrell, "Role of rare earth sites and vacancies in the anomalous compression of modulated scheelite tungstates $RE_2(WO_4)_3$," *Physical Review Materials*, vol. 5, no. 12, 123601, 2021. https://doi.org/10.1103/PhysRevMaterials.5.123601

[20] C. Guzmán-Afonso, S. F. León-Luis, J. A. Sans, C. González-Silgo, P. Rodríguez-Hernández, S. Radescu, A. Muñoz, J. López-Solano, E. Errandonea, F. J. Manjón, U. R. Rodríguez-Mendoza, and V. Lavin, "–" *J. Phys.: Condens. Matter*, vol. 27, no. 46, 465401, 2015. https://doi.org/10.1088/0953-8984/27/46/465401

[21] R. Ramesh and N. A. Spaldin, "Multiferroics: progress and prospects in thin films," *Nat. Mater.*, vol. 6, pp. 21–29, 2007. https://doi.org/10.1038/nmat1805

[22] P. Toledano and J.-C. Toledano, *Landau Theory of Phase Transitions: Application to Structural, Incommensurate, Magnetic and Liquid Crystal Systems*, World Scientific, 1987. https://doi.org/10.1142/0215

[23] W. Jeitschko, "A comprehensive X-ray study of the ferroelectric–ferroelastic and paraelectric–paraelastic phases of $Gd_2(MoO_4)_3$," *Acta Crystallogr. Sect. B*, vol. 28, pp. 60–76, 1972.

[24] I.-E. Nylund, M. Tsoutsouva, T. Grande, and D. Meier, "Observation of cation-specific critical behavior at the improper ferroelectric phase transition in $Gd_2(MoO_4)_3$," *Phys. Rev. Mater.*, vol. 6, p. 034402, 2022. https://doi.org/10.1103/PhysRevMaterials.6.034402

[25] C. Guzmán-Afonso, C. González-Silgo, M. E. Torres, E. Matesanz, and A. Mujica, "Ferroelectric transitions in rare-earth molybdates under pressure," *J. Phys.: Condens. Matter*, vol. 25, p. 035902, 2012. https://doi.org/10.1088/0953-8984/25/3/035902

[26] C. González-Silgo, C. Guzmán-Afonso, V. M. Sánchez-Fajardo, S. Acosta-Gutiérrez, A. Sánchez-Soares, M. E. Torres, *et al.*, "Polymorphism in $Ho_2(MoO_4)_3$," *Powder Diffr.*, vol. 28, S2, pp. S33–S40, 2013.

[27] G. Gil-de-Cos, M. E. Torres, and C. González-Silgo, "Investigations of structure-improper ferroelectricity relationships to enhance the multifunctional applications of the -$Y_2(MoO_4)_3$ phase," *J. Solid State Chem.*, vol. 318, p. 123738, 2023. https://doi.org/10.1016/j.jssc.2022.123738

[28] G. Gil-de-Cos, M. E. Torres, C. González-Silgo, K. Soler-Carracedo, I. R. Martín, F. Rivera-López, and S. Rodríguez-Rodríguez, "Unexpected wide tuning of ferroelectric properties by varying the Er concentration in $La_{2-x}Er_x(MoO_4)_3$ (x = 0.75, 1, 1.25) solid solutions," *J. Solid State Chem.*, vol. 315, p. 123462, 2022. https://doi.org/10.1016/j.jssc.2022.123462

[29] D. Orobengoa, C. Capillas, M. I. Aroyo, and J. M. Perez-Mato, "AMPLIMODES: symmetry-mode analysis on the Bilbao Crystallographic Server," *J. Appl. Crystallogr.*, vol. 42, p. 820, 2009. https://doi.org/10.1107/S0021889809028064

[30] C. Guzmán-Afonso, J. López-Solano, C. González-Silgo, S. F. León-Luis, E. Matesanz, and A. Mujica, "Thermoelastic properties of scheelite-type tungstates," *High Press. Res.*, vol. 34, pp. 184–190, 2014. https://doi.org/10.1080/08957959.2014.895342

[31] VMG Physics, "Crystal Symmetry || Symmetry Elements || Symmetry Operations," YouTube video, Jul. 2021. https://www.youtube.com/watch?v=Lwtz7hylnlU (accessed July 6, 2025)

[32] S. H. Simon, *The Oxford Solid State Basics*, Oxford University Press, Oxford, 2013. https://global.oup.com/academic/product/the-oxford-solid-state-basics-9780199680771

[33] Cristalografía. Dispersión y difracción. Ley de Bragg, Curso de Cristalografía, Instituto de Química-Física "Rocasolano" (IQFR-CSIC). https://www.xtal.iqf.csic.es/Cristalografia/parte_05_5.html (consultado el 6 de julio de 2025)

[34] J. Rodríguez-Carvajal, "Polymorphism in $Ho_2(MoO_4)_3$," *Powder Diffraction*, vol. 28, no. S2, pp. S33–S40, 2013. https://doi.org/10.1017/S0885715613001176

[35] E. González Correa, *Evidencias de descomposición en multiferróicos $RE_2(MoO_4)_3$ antes de PIA [Evidence of decomposition in $RE_2(MoO_4)_3$ multiferroics before PIA]*, Trabajo Fin de Grado, Universidad de La Laguna, 2021.

[36] A. Mujica, A. Rubio, A. Muñoz, and R. J. Needs, "High-pressure phases of groups-IV, II-V, and II-VI compounds," *Rev. Mod. Phys.*, vol. 75, p. 863, 2003. https://doi.org/10.1103/RevModPhys.75.863

[37] N. P. Sabalisck, J. López-Solano, C. Guzmán-Afonso, D. Santamaría-Pérez, C. González-Silgo, A. Mújica, A. Muñoz, P. Rodríguez-Hernández, S. Radescu, X. Vendrell, L. Mestres, J. A. Sans, and F. J. Manjón, "Effect of pressure on $La_2(WO_4)_3$ with a modulated scheelite-type structure," *Phys. Rev. B*, vol. 89, no. 17, p. 174112, 2014. https://doi.org/10.1103/PhysRevB.89.174112

[38] J. Hafner, "Ab-initio simulations of materials using VASP: Density-functional theory and beyond," *Journal of Computational Chemistry*, vol. 29, no. 13, pp. 2044–2078, 2008. https://doi.org/10.1002/jcc.21057

[39] Institut Laue-Langevin (ILL), "Official website of the ILL," https://www.ill.eu

[40] Centro de Apoyo a la Investigación (CAI), Universidad Complutense de Madrid, "X-ray diffraction techniques," https://cai.ucm.es/tecnicas-quimicas/difraccion-rayos-x/

[41] Institut Laue-Langevin (ILL), "What are the technical specifications of the ILL's reactor?", https://www.ill.eu/redirects/tools/faq/detail/what-are-the-technical-specifications-of-the-ills-reactor

[42] "X-ray tube illustration vector," Vecteezy, https://static.vecteezy.com/system/resources/previews/018/989/211/non_2x/x-ray-tube-illustration-vector.jpg

[43] W. C. Hamilton, "Comparison of X-ray and Neutron diffraction structural results: A study in methods of error analysis," *Acta Crystallographica Section A*, vol. 25, pp. 194–206, 1969. https://doi.org/10.1107/S0567739469000528

[44] "Electrón Auger," *Wikipedia, la enciclopedia libre*, https://es.wikipedia.org/wiki/Electr%C3%B3n_Auger

[45] "Cross section," *Wikipedia, the free encyclopedia*, https://en.wikipedia.org/wiki/Cross_section_(physics)

[46] Varley F. Sears, "Neutron scattering lengths and cross sections," *Neutron News*, vol. 3, no. 3, pp. 26–37, 1992. https://doi.org/10.1080/10448639208218770

[47] "Compton effect," *Wikipedia, the free encyclopedia*, https://en.wikipedia.org/wiki/Compton_effect

[48] S. W. Lovesey, *Theory of Neutron Scattering from Condensed Matter*, Oxford University Press, 1984. https://doi.org/10.1063/1.2815129

[49] National Institute of Standards and Technology (NIST), "Scattering length periodic table," NIST Center for Neutron Research, https://www.nist.gov/ncnr/planning-your-experiment/scattering-length-periodic-table

[50] Diamond Light Source, "Synchrotron Industry News: Powder Diffraction," https://www.diamond.ac.uk/default/industry/Industry-News/Latest-News/Synchrotron-Industry-News-Powder-Diffraction.html

[51] Institut Laue-Langevin (ILL), "Instrument layout of the D2B high-resolution powder diffractometer," https://www.ill.eu/for-ill-users/instruments/instruments-list/d2b/description/instrument-layout

[52] "Inorganic Crystal Structure Database (ICSD)," https://icsd.products.fiz-karlsruhe.de/

[53] FullProf Suite, "Data analysis program," https://www.ill.eu/sites/fullprof/

[54] L. B. McCusker, R. B. Von Dreele, D. E. Cox, D. Louer, and P. Scardi, "Rietveld refinement guidelines," *Journal of Applied Crystallography*, vol. 32, pp. 36–50, 1999. https://doi.org/10.1107/S0021889898009856

[55] P. Thompson, D. E. Cox, and J. B. Hastings, "Rietveld refinement of Debye–Scherrer synchrotron X-ray data from Al_2O_3," *Journal of Applied Crystallography*, vol. 20, pp. 79–83, 1987. https://doi.org/10.1107/S0021889887087090

[56] "Chebyshev polynomials," *Wikipedia, the free encyclopedia*, https://en.wikipedia.org/wiki/Chebyshev_polynomials

[57] C. Guzmán-Afonso, J. A. Sans, C. González-Silgo, S. F. León-Luis, E. Errandonea, D. Santamaría-Pérez, and A. Mujica, "Structural investigation of the negative thermal expansion in yttrium and rare earth molybdates," *Journal of Physics: Condensed Matter*, vol. 23, no. 32, p. 325402, 2011. https://doi.org/10.1088/0953-8984/23/32/325402

[58] C. Guzmán-Afonso, J. López-Solano, C. González-Silgo, S. F. León-Luis, E. Matesanz, and A. Mujica, "Pressure evolution of two polymorphs of $Tb_2(MoO_4)_3$," *High Pressure Research*, vol. 34, no. 2, pp. 184–190, 2014. https://doi.org/10.1080/08957959.2014.895342

[59] I. da Silva, G. Gil-de-Cos, C. Guzmán-Afonso, D. Santamaría-Pérez, C. González-Silgo, A. Mújica, A. Muñoz, P. Rodríguez-Hernández, S. Radescu, X. Vendrell, L. Mestres, J. López-Solano, J. A. Sans, and F. J. Manjón, "Solid-state synthesis and phase transitions in the $RE_2(MoO_4)_3$ family monitored by thermodiffraction," *Crystal Growth Design*, vol. 23, no. 4, pp. 2417–2429, 2023. https://doi.org/10.1021/acs.cgd.2c01387

7 Appendix

The agreement factors of the multipattern and multiphase Rietveld refinement are presented in Tables 1 and 2, each corresponding to a different temperature. The refinements were performed separately for each temperature with the goal of linking the neutron wavelength used for the three trimolybdates. Each refinement employed nine diffraction patterns: six from neutrons and three from X-rays, distributed as follows:

- **Pattern 1:** Neutrons (full detector) of $Tb_2(MoO_4)_3$
- **Pattern 2:** Neutrons (detector center) of $Tb_2(MoO_4)_3$
- **Pattern 3:** X-rays of $Tb_2(MoO_4)_3$
- **Pattern 4:** Neutrons (full detector) of $Dy_2(MoO_4)_3$
- **Pattern 5:** Neutrons (detector center) of $Dy_2(MoO_4)_3$
- **Pattern 6:** X-rays of $Dy_2(MoO_4)_3$
- **Pattern 7:** Neutrons (full detector) of $Ho_2(MoO_4)_3$
- **Pattern 8:** Neutrons (detector center) of $Ho_2(MoO_4)_3$
- **Pattern 9:** X-rays of $Ho_2(MoO_4)_3$

The phases included in the refinements were:

- **Phase 1:** β-$Tb_2(MoO_4)_3$ or β'-$Tb_2(MoO_4)_3$
- **Phase 2:** β-$Dy_2(MoO_4)_3$ or β'-$Dy_2(MoO_4)_3$
- **Phase 3:** β-$Ho_2(MoO_4)_3$ or β'-$Ho_2(MoO_4)_3$
- **Phase 4:** Aluminium
- **Phase 5:** Le Bail refinement of $Tb_2(MoO_4)_3$
- **Phase 6:** Le Bail refinement of $Dy_2(MoO_4)_3$
- **Phase 7:** Le Bail refinement of $Ho_2(MoO_4)_3$

Table 1: Representative profile agreement factors from the Rietveld refinement of rare-earth trimolybdate diffractograms at different temperatures.

	475 K			425 K			375 K			300 K			275 K			225 K		
Patrón	R_{wp}	R_{exp}	χ^2	R_{wp}	R_{exp}	χ^2	R_{wp}	R_{exp}	χ^2	R_{wp}	R_{exp}	χ^2	R_{wp}	R_{exp}	χ^2	R_{wp}	R_{exp}	χ^2
1	9.78	5.27	3.45	9.79	5.03	3.78	8.39	4.87	2.97	7.86	4.58	2.94	7.75	4.51	2.96	7.53	4.34	3.01
2	14.80	8.96	2.73	14.30	8.64	2.75	13.10	8.39	2.44	12.60	7.91	2.55	12.40	7.80	2.51	12.30	7.55	2.64
3	13.20	7.69	2.96	11.20	7.67	2.12	10.40	7.75	1.79	10.00	7.78	1.66	10.10	7.76	1.68	9.76	7.69	1.61
4	11.40	8.58	1.76	11.60	8.41	1.91	10.50	8.14	1.66	10.20	7.71	1.74	9.71	7.55	1.65	9.33	7.26	1.65
5	17.90	14.42	1.55	17.80	14.15	1.59	17.50	13.95	1.58	16.40	13.17	1.56	16.40	13.07	1.58	15.40	12.46	1.52
6	13.90	8.63	2.58	11.30	8.61	1.73	17.60	8.54	4.25	10.40	8.67	1.43	9.90	8.66	1.31	9.97	8.65	1.33
7	9.34	5.04	3.43	10.10	4.88	4.24	8.61	4.69	3.37	7.46	4.44	2.83	7.40	4.35	2.89	7.20	4.16	3.00
8	14.30	8.56	2.80	14.40	8.29	3.04	13.30	8.05	2.73	12.10	7.68	2.49	12.20	7.51	2.64	11.80	7.26	2.66
9	9.25	6.36	2.11	8.46	6.33	1.79	11.70	6.27	3.51	8.38	6.23	1.81	8.51	6.22	1.87	8.59	6.21	1.91

Table 2: Representative intensity agreement factors from the Rietveld refinement of rare-earth trimolybdate diffractograms at different temperatures.

	475 K		425 K		375 K		300 K		275 K		225 K	
Patrón	Fase	R_{Bragg}	Fase	R_{Bragg}	Fase	R_{Bragg}	Fase	R_{Bragg}	Fase	R_{Bragg}	Fase	R_{Bragg}
1	1	4.419	4	2.834	1	4.771	4	1.092	1	4.197	4	1.846
2	1	5.226	4	4.891	1	5.653	4	2.458	1	5.090	4	1.916
3	5	0.0258	–	–	5	0.0233	–	–	5	0.01219	–	–
4	2	4.655	4	4.869	2	4.973	4	5.459	2	4.137	4	3.922
5	2	5.255	4	2.239	2	5.380	4	4.104	2	5.379	4	2.239
6	6	0.0527	–	–	6	0.0809	–	–	6	0.2025	–	–
7	3	3.974	4	1.637	3	5.086	4	1.888	3	4.085	4	1.215
8	3	4.388	4	2.329	3	5.531	4	1.337	3	4.976	4	1.903
9	7	0.0090	–	–	7	0.0484	–	–	7	0.01970	–	–
1	1	3.629	4	2.028	1	3.430	4	2.008	1	3.274	4	2.307
2	1	4.354	4	2.977	1	4.390	4	3.013	1	4.260	4	3.505
3	5	0.01164	–	–	5	0.02226	–	–	5	0.01443	–	–
4	2	4.064	4	4.770	2	3.810	4	5.402	2	3.921	4	4.568
5	2	4.840	4	4.794	2	4.943	4	5.303	2	4.794	4	3.846
6	6	0.5194	–	–	6	0.08884	–	–	6	0.2198	–	–
7	3	3.049	4	1.669	3	3.037	4	1.524	3	2.813	4	1.452
8	3	4.137	4	1.671	3	3.870	4	2.266	3	3.811	4	3.010
9	7	0.00833	–	–	7	0.09323	–	–	7	0.01573	–	–